DISSERTATIONES
CHIMICAE
UNIVERSITATIS
TARTUENSIS
190

MARTIN MAIDE

Influence of the microstructure and chemical composition of the fuel electrode on the electrochemical performance of reversible solid oxide fuel cell

DISSERTATIONES CHIMICAE UNIVERSITATIS TARTUENSIS

190

DISSERTATIONES CHIMICAE UNIVERSITATIS TARTUENSIS

190

MARTIN MAIDE

Influence of the microstructure and chemical composition of the fuel electrode on the electrochemical performance of reversible solid oxide fuel cell

UNIVERSITY OF TARTU
Press

Institute of Chemistry, Faculty of Science and Technology, University of Tartu, Estonia

The dissertation is accepted for the commencement of the degree of Doctor of Philosophy in Chemistry on February 13th, 2020, by the Council of Institute of Chemistry, University of Tartu.

Supervisors: Ph.D. Gunnar Nurk
University of Tartu, Estonia

Prof. Enn Lust
University of Tartu, Estonia

Opponent: Assoc. prof. Bhaskar Reddy Sudireddy, Technical University of Denmark, Denmark

Commencement: 03.04.2020, at 14:15. Auditorium 1020, Ravila 14a, Tartu

European Union
European Regional
Development Fund

Investing
in your future

ISSN 1406-0299
ISBN 978-9949-03-298-3 (print)
ISBN 978-9949-03-299-0 (pdf)

University of Tartu Press
www.tyk.ee

TABLE OF CONTENTS

1. LIST OF ORIGINAL PUBLICATIONS

I. K. Lillmaa, M. Maide, R. Kanarbik, G. Nurk, E. Lust, Electrochemical Characteristics and Gas Composition Generated by $La_{0.8}Sr_{0.2}Cr_{0.5}Mn_{0.5}O_{3-\delta}$ Cathode at Electrolysis and Co-electrolysis Modes, J. Electrochem. Soc. 163 (11) (2016) F3190–F3196.

II. M. Maide, K. Lillmaa, L.K. Salvan, P. Möller, M. Uibu, E. Lust, G. Nurk, Influence of Electrolyte Scaffold Microstructure and Loading of MIEC Material on the Electrochemical Performance of RSOC Fuel Electrode, Fuel Cells. 18 (6) (2018) 789–799.

III. M. Maide, P. Paiste, P. Möller, E. Lust, G. Nurk, Influence of A- and B-Site Modifications of $(La_{1-x}Sr_x)_yCr_{0.5-z}Mn_{0.5-w}Ni_{z+w}O_{3-\delta}$ on Electrochemical Impedance Characteristics of Reversible Solid Oxide Cell, J. Electrochem. Soc. 166 (15) (2019) F1148–F1156.

IV. M. Maide, K. Lillmaa, G. Nurk, E. Lust, Dependence of Syngas Composition on Microstructure of $La_{0.8}Sr_{0.2}Cr_{0.5}Mn_{0.5}O_{3-\delta}$ Based Cathode for CO_2 and H_2O Co-Electrolysis, ECS Trans. 78 (1) (2017) 3275–3281.

V. M. Maide, P. Möller, G. Nurk, E. Lust, Influence of A-Site Deficiency, Porous Electrolyte Scaffold and Loading of MIEC Material on the Performance of $La_{0.8}Sr_{0.2}Cr_{0.5}Mn_{0.5}O_{3-\delta}$ Based R-SOC Fuel Electrode, ECS Trans. 91 (1) (2019) 2369–2377.

Author's contribution:

Paper I: Participated in the synthesis and electrochemical characterization of the single cells. Mainly responsible for the preparation of the manuscript.

Paper II: Performed the synthesis of the single cells, some physical and all electrochemical characterization of the single cells, and analysis of the data. Mainly responsible for the preparation of the manuscript.

Paper III: Performed the synthesis of the single cells, some physical and all electrochemical characterization of the single cells, and analysis of the data. Mainly responsible for the preparation of the manuscript.

Paper IV: Performed the synthesis of the single cells, some physical and all electrochemical characterization of the single cells, and analysis of the data. Mainly responsible for the preparation of the manuscript.

Paper V: Performed the synthesis of the single cells, some physical and all electrochemical characterization of the single cells, and analysis of the data. Mainly responsible for the preparation of the manuscript.

2. ABBREVIATIONS AND SYMBOLS

$\Delta Z'$ – the difference between the derivatives of the spectrums obtained at different hydrogen partial pressures
$\Delta Z''$ – the difference between the derivatives of the spectrums obtained at different oxygen partial pressures
ac – alternating current
ADIS – analysis of differences in impedance spectra
ASR – area-specific resistance
$C_{1,2,3}$ – capacitance of the corresponding semi-circle
$\mathrm{CPE}_{1,2,3}$ – constant-phase element of the corresponding semi-circle
CV – cyclic voltamperometry
E_a – activation energy
EC – equivalent circuit
EIS – electrochemical impedance spectroscopy
f – frequency
GDC – $Ce_{1-x}Gd_xO_{2-\delta}$
HF – high-frequency
(HT-)XRD – (High-temperature) X-ray diffraction
i – imaginary unit
I_0 – amplitude of the current
ICP-MS – inductively coupled plasma mass spectrometry
I(t) – ac current function
j – current density
L – high-frequency inductance
LF – low-frequency
LSCF – $La_{1-x}Sr_xCo_{1-y}Fe_yO_{3-\delta}$
LSCM – $La_{1-x}Sr_xCr_{1-y}Mn_yO_{3-\delta}$
LSCMN – $(La_{1-x}Sr_x)_yCr_{0.5-z}Mn_{0.5-w}Ni_{z+w}O_{3-\delta}$
LSF – $La_{1-x}Sr_xFeO_{3-\delta}$
LSGM – $La_{1-x}Sr_xGa_{1-y}Mg_yO_{3-\delta}$
LST – $La_{1-x}Sr_xTiO_{3-\delta}$
LSV – $La_{1-x}Sr_xVO_{3-\delta}$
MIEC – mixed ionic electronic conductor
OCV – open-circuit voltage
ORR – oxygen reduction reaction
P – power density
pCO_2 – the partial pressure of carbon dioxide
pH_2 – the partial pressure of hydrogen
pO_2 – the partial pressure of oxygen
$R_{1,2,3}$ – resistance of the corresponding semi-circle
R_p – polarization resistance
R_s – high-frequency ohmic resistance
RSOC – reversible solid oxide cell

RWGS – reverse water-gas shift
ScSZ – $Zr_{0.94}Sc_{0.06}O_{2-\delta}$
ScCeSZ – $Zr_{0.79}Sc_{0.20}Ce_{0.01}O_{2-\delta}$
SDC – $Ce_{1-x}Sm_xO_{2-\delta}$
SEM – scanning electron microscopy
SFM – $Sr_xFe_{1-y}Mo_yO_{6-\delta}$
SFN – $Sr_xFe_{2-y}Nb_yO_{6-\delta}$
SMgMo – $Sr_xMg_{1-y}Mo_yO_{6-\delta}$
SOC – solid oxide cell
SOEC – solid oxide electrolysis cell
SOFC – solid oxide fuel cell
TOF-SIMS – time-of-flight secondary-ion mass-spectrometry
TPB – three-phase boundary
U_0 – steady-state potential
$U(t)$ – ac potential function
WGS – water-gas shift
W_s – short-circuit Warburg impedance
YSZ – $Zr_{1-x}Y_xO_{2-\delta}$
$Z(t)$ – impedance as a function of time
$Z(\omega)$ – impedance as a function of angular frequency
Z' – the real part of the impedance
Z'' – the imaginary part of the impedance
φ – phase-shift
ω – angular frequency

3. INTRODUCTION

Due to possibly increasing energy demand, the implementation of renewable energy resources is an urgent need. A most important step toward this goal is to develop efficient, environmentally friendly devices for sustainable energy conversion and storage [1]. One of such technologies is reversible solid oxide cell (RSOC), which can work as high-temperature solid oxide fuel cell (SOFC) for fuel oxidation and as solid oxide electrolysis cell (SOEC) for fuel production from excess electricity and steam or carbon dioxide. The advantage of the mentioned systems is high electrical (up to 70%) and overall (up to 90%) efficiency as well as fuel flexibility [2]. It is a very promising technology to be used in conjunction with intermittent energy sources, e.g., solar and wind energy systems. However, it has to reach a more mature state to be implemented in the energy market, and therefore, research and development are still needed to improve reliability, lifetime and lower the cost of the systems [3].

The most commonly used anode materials for SOCs are nickel- and copper-based cermets combined with yttria-stabilized zirconia (YSZ), scandia stabilized zirconia (ScSZ) or gadolinia doped ceria (GDC) electrolytes [4,5]. However, most of the named materials are very sensitive to the redox cycles or purity (e.g., sulfur, etc.) of the electrode inlet gases and therefore tend to suffer increased degradation under standard working conditions [6,7]. Furthermore, for the nickel element catalyst, carbon deposition can be a very serious problem [8].

Therefore, mixed ionic-electronic conductive (MIEC) materials have been in focus during the last years as a promising alternative for cermets materials. High chemical stability as a potential strength of these materials, ABO_3 perovskite-type $La_{1-x}Sr_xCr_{1-y}Mn_yO_{3-\delta}$ (LSCM) [9], $La_{1-x}Sr_xTiO_{3-\delta}$ (LST) [10], $La_{1-x}Sr_xCr_{1-y}Fe_yO_{3-\delta}$ (LSCF) [11], and $La_{1-x}Sr_xVO_{3-\delta}$ (LSV) [12], or double perovskite-type $Sr_2FeNbO_{6-\delta}$ (SFN) [13] and $Sr_2FeMoO_{6-\delta}$ (SFM) [14] have been studied for SOC applications. So far, low catalytic activity and poor conductivity are still the most common throwbacks for MIEC electrodes, and therefore additional activation of these materials is necessary.

One possible solution for the activation of such materials is the infiltration of catalysts onto the surface of the MIEC electrode materials. Infiltration is extensively used in heterogeneous catalysis and has proved its value as a capable technique and without it (or using alternative methods, like thermal combustion synthesis followed by co-sintering of electrode-electrolyte systems, etc.) the preparation of many potential SOC electrode materials would not be possible [15].

Alternatively, active interfaces can also be generated *in-situ* through a phase decomposition process known as redox exsolution [16,17]. Redox exsolution allows interesting structural interplay and creation of new and exciting metal-oxide interfaces as well as the possibility to combine these with other desirable electrode functionalities, for example, mixed electronic and ionic conduction, etc. Therefore, the redox exsolution seems like an excellent method for the activation of the electrode materials due to the very diverse crystallographic properties of perovskite MIEC materials.

Additionally, the characteristics (conductivity and catalytic activity) of electrodes depend on the microstructural properties – the specific surface area, total pore volume, tortuosity, etc. of the final electrode structure, amount of MIEC in the electrolyte scaffold, etc. Therefore, the optimization of such parameters is crucial to achieving maximal power densities of SOCs [18].

The main aim of this work was to understand the influence of the electrode microstructure and chemical composition of the MIEC materials and to improve the electrochemical behavior of reversible solid oxide single cells. More specifically, the current study focused on the modifications in A- and B-site compositions of $(La_{1-x}Sr_x)_yCr_{0.5-z}Mn_{0.5-w}Ni_{z+w}O_{3-\delta}$ material as well as the influence of loading of $(La_{1-x}Sr_x)_yCr_{0.5-z}Mn_{0.5-w}Ni_{z+w}O_{3-\delta}$ and $Sr_xFe_{1-y}Mo_yO_{6-\delta}$ MIEC materials on the electrochemical behavior of reversible solid oxide single cells. Furthermore, the analysis of differences in impedance spectra (ADIS) was conducted by the variation of test conditions to understand the processes initiating established changes of impedance components in studied systems.

4. LITERATURE OVERVIEW

4.1 Design of solid oxide cell single cells

Solid oxide cell (SOC) is an all-solid-state energy conversion device that enables direct chemical energy conversion to electrical energy in fuel cell and vice versa in the electrolysis mode at elevated temperatures.

Conventional SOC consists of dense oxide ion-conducting electrolyte, located between porous electrodes (Fig. 1). Redox reactions of oxygen or oxygen-containing species take place on the air electrode, i.e., reduction of oxygen on the cathode (fuel cell mode) and oxidation of oxygen ions on the anode (electrolysis cell mode), respectively (Eq. 1).

$$O_2 + 4e^- \leftrightarrow 2O^{2-} \quad (1)$$

Similarly, redox reactions of fuel or intermediates take place on fuel electrode, i.e., oxidation of hydrogen or carbon monoxide on the anode (fuel cell) and reduction of hydrogen-or carbon-containing intermediates on the cathode (electrolysis cell), respectively (Eq. 2 and 3).

$$2H_2 + 2O^{2-} \leftrightarrow 2H_2O + 4e^- \quad (2)$$

$$2CO + 2O^{2-} \leftrightarrow 2CO_2 + 4e^- \quad (3)$$

Satisfying many criteria for efficient energy conversion devices, SOC is especially attractive for its high combined electrical and thermal cycle efficiency, fuel flexibility, conceptual simplicity (compared to other types of energy conversion cells), and environmental compatibility [19,20]. The electrical efficiency of solid oxide fuel cell (SOFC) can be up to 70%, but combined electricity and heat cogeneration cycle efficiency can be even higher, reaching 90% [20]. In principle, SOFC can be operated with zero CO_2 emissions when H_2 is used as a fuel. However, any combustible fuels, e.g., natural gas (mostly methane), various other hydrocarbons (butane, hexane, decane), and alcohols (methanol, ethanol), can be used [21].

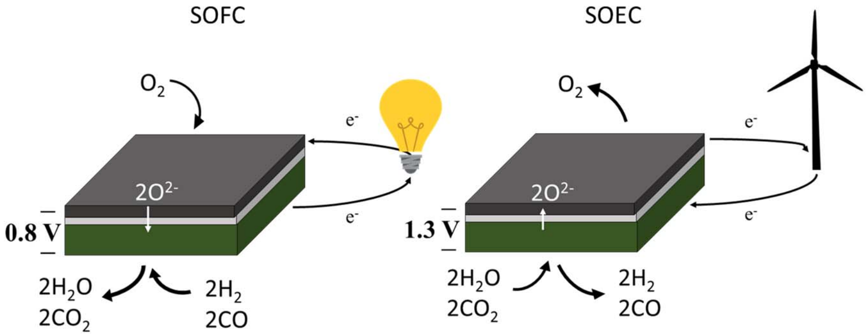

Figure 1. Illustration of the working principle of SOCs in SOFC and SOEC modes (noted in the Figure). Gray layer presents a porous oxygen electrode, the white layer thin dense electrolyte, and a green layer porous fuel electrode. The open-circuit voltage (OCV) of the SOC is around 1.1 V at 850 °C in typical operating conditions.

There are several interesting designs (configurations) for solid oxide cells, among which most popular are tubular and planar. Although the great advantage of the tubular design is the elimination of gas-tight seals in the hot zone, it still exhibits low current densities due to the long current path of electrons to the current collector. Furthermore, the planar design is conceptually simpler and less expensive in terms of fabrication methods compared to tubular design [20,22]. However, the traditional planar SOFC single cell has a thick electrolyte as a supportive element, which decreases the performance remarkably due to high ohmic losses. Fortunately, advances in ceramic processing methods have made it possible to prepare very thin electrolyte layers via screen printing, tape casting, sintering, etc. and as a result, electrolyte-supported cells with decreased ohmic resistance as well as electrode supported cells have become available [22].

The key component of solid oxide cells is a solid electrolyte, which defines several important properties of the electrode materials (chemical compatibility, thermal expansion coefficient, etc.). Yttria-stabilized-zirconia (YSZ) has been considered one of the most promising solid electrolyte material for SOFC due to its high phase stability, reasonable ionic conductivity and low electronic conductivity in both the oxidizing and reducing environments [2,20]. However, YSZ exhibits poor ionic conductivity at lower operating temperatures (< 700 °C). Therefore, wide attention has been focused on improving the ionic conductivity of the YSZ electrolyte [2]. One approach is the use of scandium oxide (Sc_2O_3) to stabilize ZrO_2 and to improve the oxide ion conductivity at lower operating temperatures. The cubic fluorite-type phase of scandia-stabilized-zirconia (ScSZ) has been reported to be an excellent electrolyte material for IT-SOFC within controlled temperature conditions.

However, ScSZ exhibits a phase transition from the highly conductive cubic phase to a low conductive rhombohedral or tetragonal phase at the IT-SOFC operating condition [23]. The use of Al_2O_3 together with the oxides of rare earth elements such as CeO_2, Sm_2O_3, Yb_2O_3, and Sc_2O_3 as dopants to mitigate the undesirable phase transition has been discussed in several studies [24–26]. In addition, some authors have reported that the phase transition of ScSZ can be prevented by the co-doping of CeO_2 [27,28]. According to the mentioned reports, the 10 mol% Sc_2O_3 – 1 mol% CeO_2 – 89 mol% ZrO_2 composition (10Sc1CeSZ) enables the retention of the highly conductive cubic phase within the SOFC operating temperature [28].

4.2 Fuel electrode materials for solid oxide fuel cells

One of the biggest advantages of SOCs is the wide variety of possible fuels, including H_2, natural gas, biogas, alcohol, gasoline, etc. [2]. The requirements for SOFC fuel electrode materials are good chemical and mechanical stability under SOFC operating conditions, high ionic (O^{2-}/H^+) and electronic conductivity over a wide range of pO_2, and good chemical and mechanical compatibility with electrolyte and interconnect materials, high surface oxygen exchange kinetics, and good catalytic properties for the anode reactions [23].

4.2.1 Cermet fuel electrode materials

The most commonly used and widely studied SOC fuel electrode materials are nickel and copper metal-ceramic composites (the so-called metal-cermets) with yttria-stabilized zirconia (YSZ), scandia stabilized zirconia (ScSZ) or gadolinia doped ceria (GDC) [4,29].

At low currents, the mentioned materials show good performance reversibility between fuel cell and electrolysis modes [30]. However, in the case of higher current densities, mentioned cells show remarkable degradation, especially in electrolysis mode [31]. The post-measurement analysis of the cells indicate that there are several reasons, for example, the presence of impurities (sulfur, ceramic nanoparticles from the electrolyte, etc.) that influence the stability of the metal catalysts. Zha et al. [32] assigned the voltage drop to both, restricted hydrogen adsorption and oxidation when sulfur is adsorbed onto the active Ni cermet catalytic centers. Furthermore, sulfur adsorption was shown to be selective (depending on the S/Ni surface ratios) at the anode surface, i.e., taking place initially at the sites of lowest coordination number (most open structure of Ni binds sulfur the strongest) [33].

Another serious issue is related to processes involving the instability of the Ni catalyst particles. The coarsening of the catalyst particles under operation conditions or mechanical stress during redox cycles due to large volume changes between metallic Ni and NiO has been observed [34,35]. Furthermore, the formation and densification of the Ni layer onto the electrolyte, an effect that is more important in high current densities in the electrolysis mode, has been proposed [4,36]. Several other degradation mechanisms have been observed and discussed by different authors, including layer peeling and microstructural changes of both fuel and oxygen electrodes [37,38].

4.2.2 Ceramic perovskite fuel electrode materials

As alternative for cermets, mixed ionic and electronic conductive (MIEC) materials have been gaining interest due to potentially reduced polarization and area-specific resistance (ASR), caused by the expansion of active reaction sites over the whole anode surface and so increasing the three-phase boundary (TPB) [39]. One big group of MIEC materials is perovskite structured oxides, which also offer excellent mechanical stability, chemical and thermodynamical compatibility with electrolyte materials, relatively low cost, and therefore, have attracted interest in their application as fuel or oxygen electrodes in SOC [40].

Traditionally, perovskite oxides possess stoichiometry ABO_3, which means that these materials comprise at least three different ionic species, each with its equilibrium defect concentration due to three different activation energies for defect formation. Combined with the constraint of electroneutrality, such materials enable diverse and potentially useful defect chemistry, particularly when considering electronic, hole, and ionic conduction under atmospheres of different oxygen partial pressures. Perovskite oxides can accommodate a large content of oxygen vacancies; hence, some perovskites are good oxygen ion conductors. The small B-site in the perovskite structure allows the first-row transition elements to be introduced in the lattice. These elements exhibit multivalency under different conditions, which may be a source of high electronic conductivity [41].

Materials such as $La_{1-x}Sr_xCr_{1-y}Mn_yO_{3-\delta}$ (LSCM) [9,42], $La_{1-x}Sr_xTiO_{3-\delta}$ (LST) [10], $La_{1-x}Sr_xCr_{1-y}Fe_yO_{3-\delta}$ (LSCF) [11] and $La_{1-x}Sr_xVO_{3-\delta}$ (LSV) [12] or double-perovskites, such as $A_2(BB')O_6$ $Sr_2FeNbO_{6-\delta}$ (SFN) and $Sr_2MgMoO_{6-\delta}$ (SMgMo) [43] have been studied for SOFCs.

Unfortunately, low catalytic activity and electronic conductivity are still the most common throwbacks for MIEC electrodes, and therefore activation of MIEC materials is needed in the future [40].

4.2.2.1 $La_{1-x}Sr_xCr_{1-y}Mn_yO_{3-\delta}$ ceramic fuel electrode material

Since its first characterization as a potential anode material, $La_{1-x}Sr_xCr_{1-y}Mn_yO_{3-\delta}$ (LSCM) has been studied as an electrode material for SOFC single cells [9,44–46]. Most of the early studies were conducted by Tao and Irvine, who established the redox stability of the LSCM electrode material [9,47]. At 900 °C, its electrical conductivity was found to be about 38 S/cm in air and 1.5 S/cm in 5% H_2 ($pO_2 \approx 10^{-21}$ atm). Rather good performance was achieved using $La_{0.75}Sr_{0.25}Cr_{0.5}Mn_{0.5}O_{3-\delta}$ anode based single cells with a polarization resistance of 0.9 and 0.47 Ω cm^2 in wet 5%H_2/Ar and wet H_2 (3% H_2O) gas compositions, respectively [9]. Further improvement in electrode microstructure decreased polarization resistance to about 0.20 Ω cm^2 in wet H_2 [47]. Some modifications of the chemical composition and A-site deficiency of the same material revealed the possible formation of spinel impurity phases to compensate for the change of cation non-stoichiometry, showing near-zero A-site deficiency in undoped material. Neutron diffraction results indicated that $La_{0.75}Sr_{0.25}Cr_{0.5}Mn_{0.5}O_{3-\delta}$ underwent a rhombohedral to a cubic phase transition from 500 to over 1000 °C, spanning over a temperature range of about 600 °C, being much wider than that previously reported for some perovskite oxides [44,48].

However, in theory, existence of dual-phase $La_{0.75}Sr_{0.25}Cr_{0.5}Mn_{0.5}O_{3-\delta}$ was not found to be a problem, as the dominant phase in the air was the same as in the reducing atmosphere, which would possibly alleviate the influence of a redox cycle in operating conditions [44].

More recent studies have characterized LSCM also in electrolysis mode [49–52]. Yue and Irvine [52,53] have studied LSCM-YSZ and LSCM-GDC fuel electrode materials for high-temperature CO_2 electrolysis. Collected results indicated that compared to the LSCM/YSZ cathode, the LSCM/GDC cathode displayed higher electrochemical impedance at OCV, while higher performance under load probably due to the reduction of GDC, which enhanced the cathode activity. Polarization resistances were around 0.8 and 0.9 Ω cm^2 at 900 °C and 50/50 CO_2/CO gas composition for LSCM/GDC and LSCM/YSZ, respectively. Still, the catalytic activity of the cells was deemed too low for the CO_2 electrolysis, and the authors recommended some improvement in fabrication methods to enable the use of the materials in real working systems [53].

The performance of the LSCM/GDC electrode was later improved by the impregnation of fine GDC particles and Pd co-catalyst into the LSCM/YSZ structure [52]. As a result, polarization resistance of about 0.3 Ω cm^2 at 900 °C and 50/50 CO_2/CO gas composition was achieved. Zhang et al. [51] impregnated the LSCM electrode with 2 wt. % of V_2O_5, decreasing polarization resistance from 2.6 to 1.2 Ω cm^2 at 800 °C in pure H_2. Ruan et al. [50] decorated the LSCM electrode with the *in-situ* grown nickel catalyst (LSCMN), achieving polarization resistances of 0.8 and 0.65 Ω cm^2 for pure LSCM and LSCMN, respectively, at 800 °C and cell potential 2.0 V in pure CO_2 gas environment. Copper activated LSCM was used to improve H_2O, and CO_2 co-electrolysis characteristics, polarization resistance around 0.3 Ω cm^2 was achieved for $H_2O/H_2/CO_2$ gas composition in a ratio of 50/12.5/37.5 at 750 °C [49].

LSCM has even been studied for use as a cathode material in the fuel cell regime. Solid-state reaction and gel-casting methods were employed to study the influence of the preparation method on the electrochemical characteristics of the single cells. The gel-casting method produced more active electrode materials toward O_2 reduction, for which the most probable reason was a more uniform sub-micron scale distribution in LSCM grain particle sizes. Analysis of the influence of calcination temperature of LSCM powders showed the best electrochemical behavior for materials produced at 1100 °C. Polarization resistance values of 0.33 and 1.45 Ω cm^2 were measured for materials prepared by gel-casting and solid-state reaction methods, respectively [54].

As already mentioned, several studies have focused on the analysis of the influence of A- and B-site composition of the material on the electrochemical activity [44,46,47,55].

So far, most studied catalysts for LSCM activation include Ni, Cu, Pd, Pt, V_2O_5, CeO_2 [51,56–58]. Kim et al. [56] showed that in the case of methane (fuel), a large number of carbon residues with filamentous and granular structures were deposited onto the anodes containing Ni- and Pd catalysts. Anodes containing Pt exhibited high hydrocarbon tolerance, and negligible amounts of carbon were deposited upon exposure to CH_4 at 800 °C. For Ni and Pd containing electrodes, the addition of CeO_2 caused a significant decrease in the extent of carbon deposition [56]. However, Ni still seems like the most widely used catalyst for SOFC mode, as it is an excellent H_2 oxidation catalyst [59]. In the case of CO_2 electrolysis conditions, either Ce or Cu based catalysts seem to be more specific towards the reduction of CO_2 [49,52].

4.2.2.2 The $Sr_xFe_{1-y}Mo_yO_{6-\delta}$ ceramic fuel electrode material

In addition to common ABO_3 structures, a subclass of perovskites exists with a general formula of $A_2B'B''O_6$. In this case, if the difference in ionic radii of two different B site cations is large enough, the crystal lattice of such perovskite becomes ordered in a superstructure, forming primitive cells with larger unit-cell parameters than usual perovskite structures [60]. From the catalytic point of view, the specific arrangement of different B-site cations in the electrode materials can be of great interest, since the properties of perovskites as catalysts are generally determined by the nature, oxidation states and relative arrangement of B-site cations. For example, such oxide systems can consist of interesting combinations of oxygen and/or cation stoichiometries, as well as mixed-valence states of the same elements [61]. Although initially studied for their room-temperature half-metallicity and intergrain tunneling magnetoresistance effects, more recent studies have found several compositions suitable for SOFC anode materials [43,62,63].

Liu et al. [64] showed some very promising results using $Sr_2Fe_{1.5}Mo_{0.5}O_{6-\delta}$ (SFM) double-perovskite based half cells. Very high conductivity values of 550 and 310 S cm^{-1} were measured in air and hydrogen at 780 °C, respectively. Furthermore, symmetrical cells showed polarization resistances of 0.37 and 0.77 Ω cm^2 in wet H_2 and CH_4 at 900 °C, respectively. Shortly after, the same symmetrical cells were studied in the electrolysis mode. Again, promising results were achieved, whereas area-specific resistance of 0.56 and polarization resistance of 0.26 Ω cm^2 was achieved in H_2 containing 60 vol.% H_2O (absolute humidity) at 900 °C, respectively [43].

The SFM material was further improved by the addition of $Sm_{0.2}Ce_{0.8}O_{1.9}$ (SDC) completing $La_{1-x}Sr_xGa_{1-x}Mg_xO_{3-\delta}$ (LSGM) electrolyte supported cell.

Polarization resistance was reduced from 0.84 to 0.45 Ω cm^2 in wet H_2 at 700 °C when 30 wt.% of SDC was added to the electrode [44]. In addition, polarization resistance of 0.48 Ω cm^2 in the gas mixture containing $H_2O/CO_2/H_2/N_2$ in a ratio of 16/16/20/48 was achieved in co-electrolysis mode using SFM-SDC symmetrical cells at 850 °C [67].

Only recently, doping SFM with different catalysts has become popular. Doping has shown to increase the stability of different strontium molybdenum perovskites through the stabilization of M-O bonds [68,69]. Furthermore, it has been shown for SFM to tune the distribution between of Fe^{2+}/Fe^{3+} and Mo^{6+}/Mo^{5+} redox pairs [70]. Most studied catalysts for SFM activation include Ni [71,72], Nb [70], Sc [73] and Sn [74].

4.3 Electrode preparation and activation methods

4.3.1 Preparation of electrode using infiltration method

Infiltration, a technique extensively used in the field of heterogeneous catalysis to immobilize high surface area catalytic particles onto ceramic support materials, such as alumina, silica, and zirconia, has been exploited to enhance and modify SOC electrodes [15].

Infiltration requires at least one mechanically strong and porous component, or backbone, which is processed using the conventional high-temperature ceramic route. Such a so-called “scaffold” is often made by an electrolyte (stabilized zirconia or doped ceria). The flexibility that infiltration offers in terms of combining various electrode functionalities (i.e. mechanical support, ionic conductivity, electronic conductivity, oxidation/reduction electrocatalyst) has led to many researchers adopting this approach in SOC development [75].

The infiltration method also gives many advantages, like relatively low electrode fabrication temperature due to the pre-sintering of the electrolyte material and, therefore, easy control of the microstructure of the deposited materials [56]. Still, electrode fabrication by infiltration is relatively new, and there are some manufacturing issues that need to be resolved. For example, the amount of material that can be added in a single step using salt solutions is rather low, resulting in repeated infiltration-decomposition steps, which is very time consuming [76]. Furthermore, control over microstructure and its long term stability still raises questions about its readiness for industrial use [77]. Due to the large surface area of impregnated particles, microstructural coarsening is a particular and important problem under typical SOC operation conditions [75].

4.3.2 Electrode activation using infiltration method

In addition to the preparation of SOC composite electrodes, infiltration can also be used for the activation of the same materials. Most commonly, precursor solutions of the catalytically active phases are used to wet the surface of the support, which is beforehand prepared by infiltration as well. The microstructure of the final material is obtained after drying and decomposition of the precursor, developing the nanosized metal or metal oxide particles on the support material. Sometimes, the following reduction is required to create an active metal catalyst particles. Due to the high surface area nature of the nanosized catalyst, small loadings of typically 1–10 wt. % are required to have increased material activity [78,79]. This method has become very popular to activate both the fuel and oxygen electrodes. For example, the catalytic activity of LSCF is limited by the surface catalytic properties. Thus, the infiltration of doped ceria onto the LSCF cathode may partially serve to increase the surface exchange rate of oxygen as well as increase surface area of the electrode, and therefore, infiltration improves the ORR kinetics of the LSCF cathode [80]. Similarly, Kim et al. [81] used variety of catalysts, including Pd, Rh, Ni, Fe, or CeO_2, to activate YSZ-LSCM composite electrode material. Results indicated that 0.5-1 wt. % of Pd, Rh, and Ni increased the maximum power density of activated single cells over 500 mW/cm^2. However, the addition of 1 and 5 wt. % of Fe and CeO_2, respectively, had a smaller positive effect on the maximum power density of the cells. Similar enhancements have been shown for other MIEC electrodes, including LST [82] and $BaCe_{1-x}Pd_xO_{3-\delta}$ [83].

4.3.3 Electrode activation using redox exsolution

Although the most active interfaces are formed ex-situ by generating desired phases through repeated deposition processes (infiltration, etc.), interfaces with similar activity can also be generated in situ, at the beginning of the operation, through a phase decomposition process known as redox exsolution [16,17]. The catalytically active transition metals can be incorporated into the structure in oxidizing conditions, and exsolved onto the host structure in the reducing environment [17].

Due to their unique property to accommodate defects of different size, charge, and nature, the most well-studied redox exsolution processes discussed until now are performed on perovskites [84].

So far, it has been shown that redox exsolution from perovskites is a phase decomposition process occurring due to the reduction step and mainly controlled by bulk and surface defects [17,85,86]. During the reduction, perovskite lattice loses oxygen and gains electrons until the nucleation of the cation, initially located in B-site of the perovskite lattice, to metallic phase becomes favorable. Nucleation occurs on the surface of the host lattice, where the nucleation barrier is lower due to crystal defects [85,86].

Cation diffusion to the surface seems to play a most important part to sustain exsolution, as during this process, reducible ions from typically at least 100 nm deep layer emerge on the surface to form metal particles [85].

Furthermore, A-site and oxygen vacancies seem not only to drive cation and oxygen transport to the material surface but also influence the nucleation of B-site cation to the metallic phase. Vacancies facilitate ion diffusion by minimizing lattice collisions and supply hopping sites [85], which, in turn, creates a B-site excess [17]. To retain stable stoichiometry in the crystal lattice, catalytically active species diffuse to the surface and undergo a reduction [17]. Exsolved particles maintain some crystallographic coherence with initial lattice, thus becoming partly socketed, which depending on the material, can give rise to lattice strain [17,85].

In conclusion, redox exsolution allows interesting structural interplay and creation of new and exciting metal-oxide interfaces as well as the possibility to combine these with other desirable electrode functionalities, for example, mixed electronic and ionic conduction, etc. Discussed possibilities open up new dimensions in the preparation of functional materials for various devices [87].

4.4 Influence of electrode microstructure on single-cell performance

The performance of MIEC electrodes can be increased further by carefully designing and manipulating of the detailed microstructure of the electrode. Typically, this step causes increasing electrocatalytic activity, i.e., the increase of the surface area of the effective reaction zone of the electrode. As electrocatalytic activity is related to the chemical composition of the electrode, the effective reaction zone is mostly determined by the three-phase boundary (TPB) length [64,88]. However, it has been shown that the pore size, pore volume fraction, TPB length, and tortuosity are all influencing the electrochemical performance of SOFCs and are considered as the crucial parameters [18].

Additionally, the characteristics (conductivity and catalytic activity) of electrode depend on the microstructural properties – the specific surface area, total pore volume, tortuosity, etc. of the final electrode structure, amount of MIEC in the electrolyte scaffold, etc. There are several different ways to optimize the porous structures of electrodes. One of those includes the use of pore formers.

As discussed by different authors, there is some dependence between the shape and size of the pore formers and resulting pores as well as a certain threshold of pore former volume fraction, which enables the interconnection of those pores [89–91]. Alternatively, pre-treated raw oxides with various particle size distributions can be used [92–94]. Möller et al. [94] found that microstructure had a significant influence on the cell performance in the case of $La_{0.6}Sr_{0.4}CoO_{3-\delta}$ half-cells prepared from raw cathode powders with different particle size distributions.

Furthermore, Hussain et al. [95] showed that in the case of infiltrated electrodes resulting gas diffusion impedance had a clear dependency on the structural parameters of the electrodes in fuel cell mode. As indicated by

Ebbesen et al. [96], the influence of gas diffusion characteristics, depending on the microstructure of the electrode, might be even more important in the case of electrolysis mode compared to the fuel cell mode. They demonstrated that some change of porosity of support structure resulted in a significant change in the charge transfer resistance values, but however, there is the well-expressed influence of the low-frequency resistance related to mass transport kinetics at high current densities. Consequently, the morphology of porous electrolyte scaffold, amount of MIEC deposited in electrolyte scaffolds, as well as applied pre-treatment conditions of both components influence the microstructure of electrodes, hence the electrochemical activity of the reversible solid oxide cells.

4.5 Methods for electrochemical characterization of SOFCs

The most common techniques for electrochemical characterization of SOFCs are cyclic voltammetry and electrochemical impedance spectroscopy [97,98].

4.5.1 Cyclic voltammetry

The cyclic voltammetry (CV) method has become a very popular technique for initial electrochemical studies of new systems and has proven very useful in obtaining information about fairly complicated electrode reactions [97]. As the name implies, CV is a reversal electrochemical characterization technique, where the potential of the system is linearly swept in time, and the current-potential curve is recorded, as illustrated in Figure 2. In the case of ideal conditions (systems without any energy losses), the constant potential and linear increase of power of the cell would be expected.

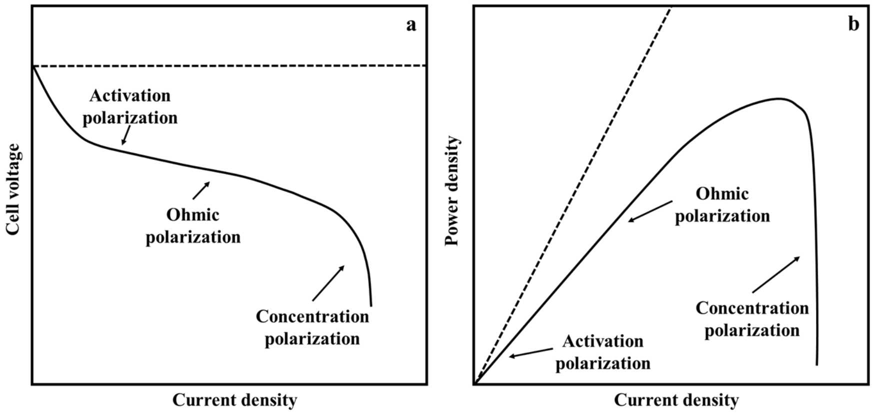

Figure 2. Typical cell current vs. cell voltage (a) and cell current vs. cell power (b) dependencies in ideal (dashed lines) and real SOC operation (continuous lines) conditions.

Unfortunately, in real systems, several processes dictate the losses of energy. At low current densities, activation polarization, which is related to the charge transfer step caused by some kinetically limited rate-determining step in electrode reactions, is important. The slow step could be the sorption of reactants-products, electron transfer, or any other reaction related process. Furthermore, the rate of the reaction is influenced by temperature, pressure, and electrode material. As SOFCs operate at high temperatures, usually reactions are rapid, and as a result, activation polarization is small.

Caused by ohmic resistance of membrane, electrodes, and current collectors, ohmic polarization arises in medium current densities.

At high current densities, the system's resistance is controlled by the mass transport rate in the gas phase and porous matrix of the electrode, and usually, a rapid decrease in cell voltage (power) will appear [20].

From current density vs. cell potential dependence, the power density, P, can be calculated:

$$P = Ej, \tag{4}$$

where j is the current density, and E is the corresponding cell potential of the system studied. As discussed earlier, for real working systems, dependence of the power density on the cell potential differs from the predicted ideal relationship [20].

4.5.2 Electrochemical impedance spectroscopy

Electrochemical impedance spectroscopy (EIS) is a powerful method for the characterization of the electrical properties of materials and their interfaces. It may be used to investigate the dynamics of bound or mobile charge carriers in the bulk or interfacial regions of any solid or liquid material: ionic, semiconducting, mixed electronic–ionic, and even insulators (dielectrics) [98].

EIS experiment involves excitation of the system under study with steady-state potential and low-amplitude alternating (ac) potential, following the measurement of phase shift and amplitude of the resulting current. Perturbation signal can be expressed as:

$$U(t) = U_0 \sin(\omega t), \tag{5}$$

where U(t) is ac potential function on time, U_0 is steady-state potential, $\omega = 2\pi$f, f is the frequency. The corresponding current is then expressed as:

$$I(t) = I_0 \sin(\omega t - \varphi) \tag{6}$$

where I(t) is ac current function on time, I_0 is the maximum amplitude of the current, and φ is the phase-shift between the voltage and current waveforms.

The impedance, which is the relationship between applied ac potential and the resulting alternating current, can be expressed as:

$$Z(t) = \frac{U(t)}{I(t)} \tag{7}$$

where Z(t) is the impedance as the function of time. As evident, impedance has both magnitude and a phase-shift φ, which makes it a vector quantity. Most commonly, impedance is measured for a large set of frequencies and can be expressed by a complex number of the vector sum of real (Z') and imaginary (Z") parts:

$$Z(\omega) = Z'(\omega) + iZ''(\omega), \tag{8}$$

where $i = \sqrt{-1}$. Dependence of the real part plotted against the imaginary part is expressed as a Nyquist plot (Figure 3).

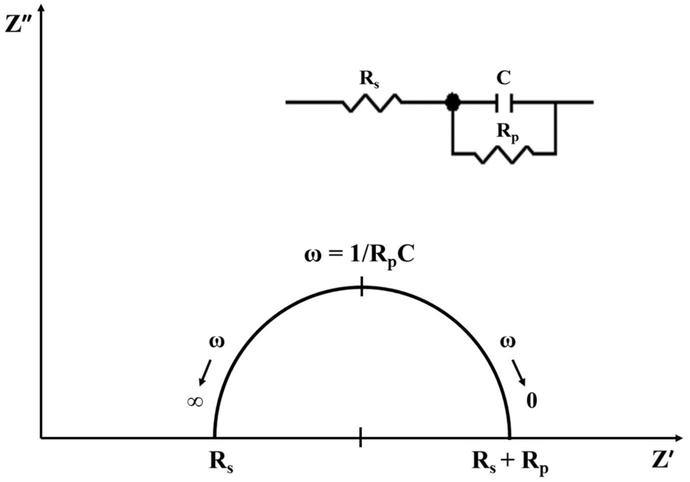

Figure 3. Typical equivalent circuit and a corresponding Nyquist plot [97].

For SOFC, first intercept at relatively higher frequencies usually corresponds to the so-called high-frequency series- or ohmic resistance, R_s, mainly caused by the resistance of the dense ion-conducting electrolyte. The resistance between high and low-frequency intercepts of the x-axis corresponds to the so-called polarization resistance, R_p, that combines all of the reactions resistances taking place at the electrodes, including adsorption, charge-transfer, and mass transfer steps of the chemical species. Depending on the values of time constants of different processes occurring in the studied systems, the Nyquist plot may contain one or multiple semi-circles [21].

4.5.3 Fitting of impedance spectra

To improve the SOFC properties, it is important to understand the reasons for activity losses and degradation mechanisms within the system. EIS has great capabilities to provide insight into which component and/or process primarily changes during SOFC/SOEC operation. It is common for the impedance of SOFC/SOEC electrodes to primarily be evaluated by a fairly primitive approach using a series of suppressed semi-circles and ascribing those to a specific reaction or process like in a corresponding equivalent electrical circuit (EC). Such an EC analysis method is usually based on the physical processes and reactions steps of interfaces discussed elsewhere [97,98]. Figure 4 shows some most commonly used ECs in SOFCs (I-III) [99–101]:

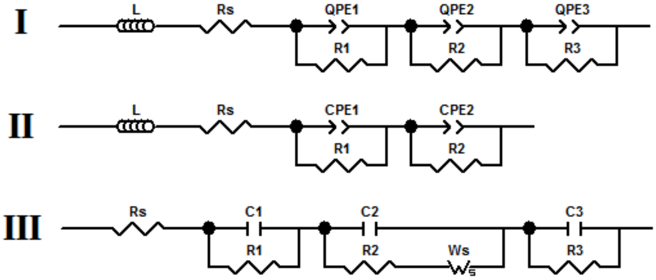

Figure 4. Equivalent circuits used for fitting of experimental impedance spectra.

However, often, such approximations can be questionable due to the coupling (overlapping) of processes, for example, diffusion followed by a reaction (Finite-Length-Warburg) or de Levie response of porous electrode describing the coupling between ionic conduction in the electrolyte and a reaction [102]. So, one has to take some caution when modeling such complicated systems.

4.5.4 Analysis of differences in impedance spectra

An empirical analysis of differences in impedance spectra (ADIS) has been proposed by different authors [100,103]. As stated before, the impedance of SOFC single cell is influenced by many processes, and very often, a separation between those various electrode processes can be quite complicated. In order to understand single-cell characteristics, however, one needs a better understanding of those processes and how they influence the impedance of the cell (or electrode material). ADIS method applies differentiation between two impedance curves, from which, the first curve is recorded before at known conditions and the second curve right after the change in some operating parameters. As a result, change in either the real ($\Delta Z'$), or imaginary ($\Delta Z''$) part of impedance influenced by the same parameter can be extracted for a set of frequencies [100].

Barfod et al. [103] used the ADIS method to convolute processes into anodic and cathodic contributions. It is highly likely that anodic processes correspond to the frequency range, which is mostly influenced by a change of the partial pressure of hydrogen in the fuel electrode compartment at constant gas flow conditions. Difference between the derivatives of the spectra (further noted as ΔZ) at different hydrogen partial pressures are expressed as:

$$\Delta Z'_{anodic} = \frac{\partial|Z_{p1(H_2)}|}{\partial \log f} - \frac{\partial|Z_{p2(H_2)}|}{\partial \log f}, \tag{9}$$

where $\Delta Z'_{anodic}$ denotes the difference in impedance real part, and $\frac{\partial|Z_{p1(H_2)}|}{\partial \log f}$ and $\frac{\partial|Z_{p2(H_2)}|}{\partial \log f}$ correspond to derivatives of the impedance spectra at different hydrogen partial pressures, respectively. $\Delta Z'_{anodic}$ vs. frequency dependencies can reveal frequency range, where anodic processes occur [101,103].

For cathodic processes, a similar difference in derivatives can be expressed:

$$\Delta Z'_{cathodic} = \frac{\partial|Z_{p1(O_2)}|}{\partial \log f} - \frac{\partial|Z_{p2(O_2)}|}{\partial \log f} \tag{10}$$

where $\Delta Z'_{cathodic}$ denotes the difference in impedance real part, and $\frac{\partial|Z_{p1(O_2)}|}{\partial \log f}$ and $\frac{\partial|Z_{p2(O_2)}|}{\partial \log f}$ correspond to derivatives of the impedance spectra at different hydrogen partial pressures, respectively.

Very often, the ADIS method requires some pre-knowledge of the processes taking place in the studied systems. Therefore, one should have prior knowledge from the literature on the possible frequency ranges of the reactions as well as their dependence on established changeable parameters, which can then simplify and accelerate the analysis of the studied system.

5. EXPERIMENTAL

5.1 Preparation of single cells

Electrolyte supported single cells used in this work were all prepared under well-controlled conditions, using tape casting, lamination, and infiltration methods. The tapes used to prepare porous and dense electrolyte layers were prepared from the slurry based on the organic solvents or solvent mixtures.

For the dense electrolyte layer, tapes were prepared using commercial $(Sc_2O_3)_{0.10}(ZrO_2)_{0.90}$ (ScSZr) (fuelcellmaterials, S_{BET}=9.0 m^2g^{-1}) and $(Sc_2O_3)_{0.10}(CeO_2)_{0.01}(ZrO_2)_{0.89}$ (ScCeSZr) (fuelcellmaterials, S_{BET}=10.6 m^2g^{-1}) electrolyte powders. Tape-casting slurry was prepared by mixing either ScSZr or ScCeSZr electrolyte powders, a mixture of solvents (ethanol and xylene in a weight ratio of 17:10) and dispersant (Menhaden fish oil, Sigma) in a weight ratio 30:23:1, respectively, and ball-milled for 24 h. After that, the binder (polyvinyl butyral B-98, Sigma-Aldrich) was added to the mixture in a weight ratio 2:27 and homogenized for additional 24 h before adding the plasticizers (polyethylene glycol 400 MW, Aldrich; benzyl butyl phthalate, Merck) in a weight ratio 3:56 and ball-milled for another 24 h. The degasification of the paste was achieved by the very slow rotation of a ball-milling vessel at least for 24 h. The green tapes were cast onto Teflon tape using a tape-casting system from MTI Corporation (AFA I Automatic Thick Film Coater).

The tapes used for the formation of porous electrolyte scaffolds were prepared similarly to dense layers using pre-calcinated electrolyte powder, as well as pore former and solvent mixtures with ethanol-to-xylene ratio 2.5:10, were added to the slurry. The main aim was the preparation of the porous structures with different porosities and pore size distributions. For this purpose, two different approaches were combined to prepare electrodes with various pore sizes – (i) pre-sintering of electrolyte powder to influence the particle size distribution of electrolyte powder and (ii) adding a controlled amount of carbonaceous pore formers with different particle size distributions to influence the size and shape of formed pores. Spherical activated carbon particles (Strem 06-0100), fractions of lamellar graphite 1 (AE-028, TIMCAL), and lamellar graphite 2 (Fluka 78391) with particle sizes up to 20 μm were used as the pore formers to obtain different types of porous scaffolds.

Dense ScSZ and ScCeSZ electrolyte layers were sandwiched and co-sintered between two porous ScCeSZ layers at 1400 °C for five hours. $(La_{1-x}Sr_x)_yCr_{0.5-z}Mn_{0.5-w}Ni_{z+w}O_{3-\delta}$ (LSCMN), and $Sr_2Fe_{1.5}Mo_{0.5}O_{6-\delta}$ (SFM) fuel and $La_{0.8}Sr_{0.2}FeO_{3-\delta}$ (LSF) oxygen electrodes were fabricated by impregnating the porous electrolyte scaffolds with aqueous solutions of corresponding salts with stoichiometric proportions. The raw solution for preparation of LSCM and SFM fuel electrodes consisted of $La(NO_3)_3\cdot6H_2O$ (99.9%, Alfa Aesar), $Sr(NO_3)_2$ (99.9%, Alfa Aesar), $Cr(NO_3)_3\cdot9H_2O$ (98.5%, Alfa Aesar), $Mn(NO_3)_2\cdot xH_2O$ (99.9%, Alfa Aesar), $Fe(NO_3)_3\cdot9H_2O$ (99.9%, Alfa Aesar), $(NH_4)_6Mo_7O_{24}\cdot4H_2O$ (99.0%, Sigma-Aldrich), and $Ni(NO_3)_2\cdot6H_2O$ (99.999%, Sigma-Aldrich) and LSF oxygen electrode raw solution consisted of $La(NO_3)_3 \cdot 6H_2O$ (99.9%, Alfa Aesar), $Sr(NO_3)_2$ (99.9%, Alfa Aesar) and $Fe(NO_3)_3 \cdot 9H_2O$ (99.9%, Alfa Aesar). Citric acid was used as a complexing agent for all aqueous solutions to assist the formation of the perovskite phase at lower synthesis temperatures in a molar 1:1 ratio (relative to metal cations). Table I shows the exact stoichiometries of raw solutions that were determined by inductively coupled plasma mass spectrometry (ICP-MS) and 8800 QQQ ICP-MS (Agilent) spectrometer. Each impregnation step was followed by a 0.5 h heat treatment step at 450 °C to decompose the selected and deposited nitrates. This procedure was repeated until the desired mass loadings of 10–50 and 35 wt. % for fuel and oxygen electrodes, respectively [21, 47] were achieved. As a final step, SFM, LSCM, and LSF were heat-treated at 900, 1100, and 900 °C, respectively, for five hours to finish the decomposition of salts and sinter the MIEC material. It should be noted that in all cases under study, the electrode with higher sintering temperature was prepared before the electrode with lower sintering temperature. Thereafter, ~3 wt% CeO_2 and ~1 wt% Pd catalysts were deposited onto the ceramic anode by infiltration of 1 M $Ce(NO_3)_3$ (99.9%, Alfa Aesar) and 0.45 M tetraammine palladium (II) nitrate (99.9%, Alfa Aesar) and heat-treated at 450 °C as a final step (publication I). Figure 5 shows a scheme for SOFC preparation by tape casting, lamination, and infiltration methods [105,106].

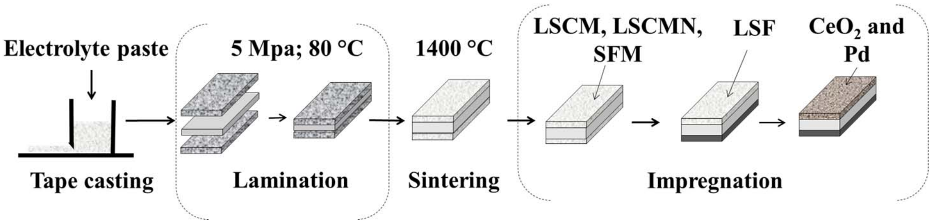

Figure 5. Scheme of SOFC preparation technique using tape casting, lamination, and infiltration methods.

5.2 Physical characterization methods

5.2.1 Inductively coupled plasma mass spectrometry

Correct stoichiometry of aqueous solution used for the preparation of electrodes was studied before the infiltration into a porous electrolyte scaffold using Agilent 8800 QQQ ICP mass spectrometer. Experimental stoichiometry was calculated based on the measured concentrations of La^{4+}, Sr^{2+}, Cr^{3+}, Mn^{3+}, Ni^{2+}, $Fe^{2+,}$ and later corrected by adding missing proportions of ions to obtain a solution close to theoretical stoichiometry, as shown in Table I. The relative standard deviation was between 0.2-2.0% throughout the measurements.

Table I. Theoretical and ICP-MS measured final cation concentrations of nitrate solutions used to prepare $(La_{1-x}Sr_x)_yCr_{0.5-z}Mn_{0.5-w}Ni_{z+w}O_{3-\delta}$ electrode materials (noted in the table) used in the publications I–III.

Material	**La [mol%]**	**Sr [mol%]**	**Cr [mol%]**	**Mn [mol%]**	**Ni [mol%]**
$La_{0.80}Sr_{0.20}Cr_{0.50}Mn_{0.50}O_{3-\delta}$	0.796	0.197	0.496	0.507	-
$(La_{0.8}Sr_{0.2})_{0.80}Cr_{0.49}Mn_{0.49}Ni_{0.02}O_{3-\delta}$	0.636	0.157	0.486	0.496	0.021
$(La_{0.8}Sr_{0.2})_{0.90}Cr_{0.49}Mn_{0.49}Ni_{0.02}O_{3-\delta}$	0.718	0.177	0.486	0.496	0.021
$(La_{0.8}Sr_{0.2})_{0.95}Cr_{0.49}Mn_{0.49}Ni_{0.02}O_{3-\delta}$	0.762	0.189	0.488	0.494	0.020
$La_{0.75}Sr_{0.25}Cr_{0.50}Mn_{0.30}Ni_{0.20}O_{3-\delta}$	0.744	0.251	0.503	0.308	0.202
$La_{0.75}Sr_{0.25}Cr_{0.30}Mn_{0.50}Ni_{0.20}O_{3-\delta}$	0.742	0.25	0.309	0.507	0.201

5.2.2 Gas chromatography

Outlet gas composition of fuel electrode was studied using Perkin Elmer Clarus 680 equipped with the Molsieve Elite column (length 30 m, diameter 0.35 mm). H_2, CH_4, and CO concentrations were established with determination levels of 1.6, 0.24, and 0.2 ml min^{-1}, respectively.

5.2.3 X-ray diffraction

X-ray diffraction (XRD) analysis of the prepared materials was carried out using Bruker D8 Advanced Diffractometer with Cu Kα1 radiation (λ=1.540596 Å), Vario1 focusing primary monochromator, two 2.5° Soller slits and a LynxEye line detector.

5.2.4 Scanning electron microscopy

Completed porous electrolyte scaffolds and single cells were characterized using Zeiss EVO® MA 15 scanning electron microscope (SEM). For more detailed information, Helios™ NanoLab 600 (FEI) high-resolution SEM was used.

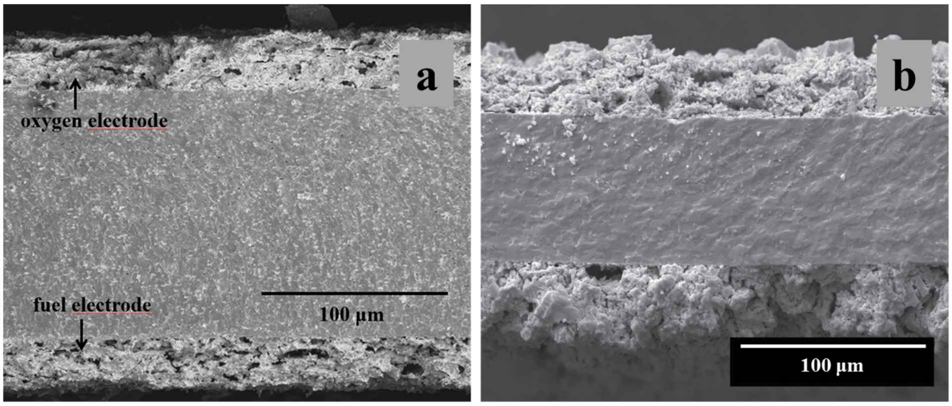

Figure 6. Cross-section of LSF|ScSZ|Pd-CeO_2-LSCM (a) and LSF|ScCeSZ|SFM (b) single cells used in publications I (a) and II (b), respectively [107,108].

5.2.5 Time-of-flight secondary ion mass spectrometry

Cross-sections of single cells were analyzed using time-of-flight secondary ion mass spectrometry (TOF-SIMS) and PHI TRIFT V nanoTOF spectrometer. A positive primary Ga+ ion beam and an accelerating voltage of 30 keV was applied. The 200×200 µm raster was used for data collection, concentration profiles of La^{4+}, Sr^{2+}, Cr^{3+}, Mn^{2+} cations were characterized in ScCeSZr electrolyte material [107].

5.3 Electrochemical characterization

5.3.1 Impedance spectroscopy

Two-electrode cell configuration was used for electrochemical measurements of the single cells prepared. Stencil printed striped Au and Ag current collectors and wires of corresponding material were used to avoid extra electrochemical activity and minimize surface area. All electrochemical measurements were carried out using a Solartron 1260 frequency response analyzer in conjunction with a Solartron 1287A potentiostat/galvanostat electrochemical interface. Polarization curves were measured from 0.7 V to 1.5 V. Impedance spectra, with AC voltage amplitude of 10 mV and within the frequency range from 10^6 to 10^{-1} Hz, were recorded under certain fixed cell potentials within potential range from 0.7 V to 1.5 V. The working temperature of the single cells was varied from 650 °C to 850 °C [100–102].

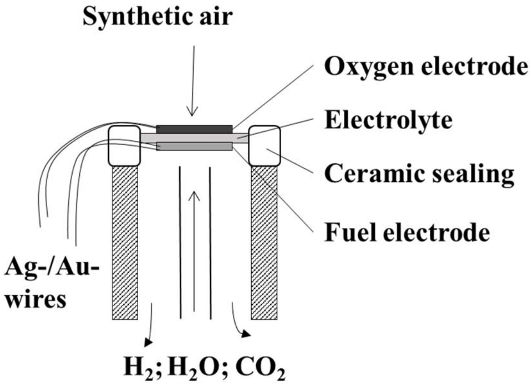

Figure 7. Experimental setup for the electrochemical characterization of systems used in this work.

6. RESULTS AND DISCUSSION

6.1 Influence of the variation of test conditions on the impedance components of SOCs

6.1.1 Influence of hydrogen partial pressure in fuel gas on the single-cell impedance in fuel cell mode

Figures 8 demonstrates Nyquist plots (Fig. 8), and Figure 9 differences of the real part of impedance spectra, ΔZ′, caused by the decrease of hydrogen concentration in the fuel compartment (Fig. 9 a and b) at OCV (Fig. 8a, 9a) and at fixed 0.8 V cell potential (Fig. 9b). Furthermore, Arrhenius plots have been shown in Figure 9c for $La_{0.8}Sr_{0.2}Cr_{0.5}Mn_{0.5}O_{3-\delta}$ (LSCM)|ScCeSZ|$La_{0.8}Sr_{0.2}FeO_{3-\delta}$ (LSF) unit cell from 700 to 850 °C at OCV [110].

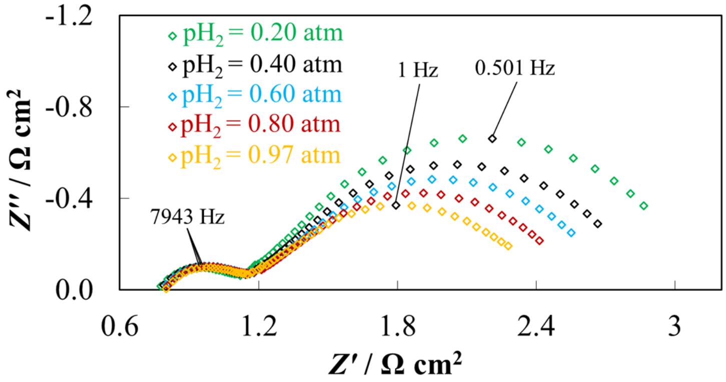

Figure 8. Nyquist plots for LSCM|CeScSZ|LSF unit cell at different hydrogen partial pressures (given in the Figure) at OCV and constant pH_2O of 0.03 atm.

At both cell potentials, the decrease of H_2 concentration led to a significant increase of ΔZ′ at frequencies below 5 Hz. Maximal impedance change appears at 0.5 Hz. According to literature data, the limiting process at 0.5 Hz range at OCV is caused by limitations of gas-solid adsorption-desorption steps (limited by the number of active adsorption sites) [99,111]. The gas conversion impedance [112] should also be considered; however, it is unlikely as the activation energy of the low-frequency process, $E_{a,\ low}$, was significantly positive [111]. The dependence of $E_{a,\ low}$ on fuel gas concentration ,pH_2, was very slight (103.3 kJ·mol^{-1}; 104.6 kJ·mol^{-1} and 103.5 kJ·mol^{-1} at pH_2=0.97; 0.8; 0.6 atm, respectively). $E_{a,\ low}$ started slightly to increase only at rather low pH_2 values of 0.4 and 0.2 (105.7 kJ·mol^{-1} and 109.4 kJ·mol^{-1}, respectively) (Figure 9c).

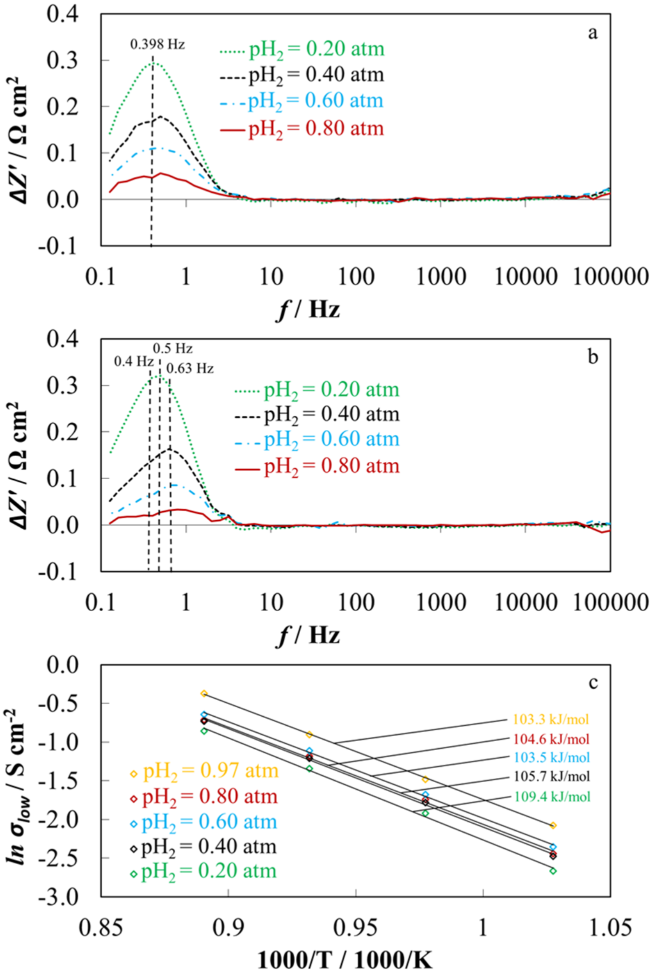

Figure 9. Differences of real part of impedance spectra, ΔZ′, at OCV (a) and at 0.8 V (b) unit cell potentials at 850 °C for LSCM|CeScSZ|LSF unit cell for hydrogen partial pressure change from pH$_2$ = 0.97 to one shown in the Figure. pH$_2$O was kept constant at 0.03 atm. Arrhenius plots (Fig. 9c) at different hydrogen partial pressures (given in the Figure) from 700 to 850 °C at OCV.

The characteristic frequency of the limiting process is only slightly influenced by the gas composition with a tendency to increase simultaneously with the increase of hydrogen concentration in the fuel compartment at OCV (no gas concentration gradient across the electrode). A comparison of data in Figure 9 a and b parts shows that compared to data at OCV, bigger shift of ΔZ′ maximum (caused by the change of pH$_2$) was observed if the pH$_2$ was changed at 0.8 V. It should be noted that at OCV, the ΔZ′ maximum frequency shifts from 0.4 Hz to 0.8 Hz, but at 0.8 V the characteristic frequency shifts from 0.4 to 1.1 Hz if pH$_2$

increases from 0.2 to 0.8 atm. The shift of characteristic frequency and ΔZ′ maximum to lower values as pH_2 decreases at 0.8 V is probably the result of simultaneous change in resistive and capacitive behavior of the MIEC composite electrode. Usually, an increase of pO_2 (if pH_2 decreases) (at 0.8 V) leads to decrease of ion vacancies in electrode material crystal lattice and, therefore to the simultaneous increase in Z′ as the conductivity of the material decreases, and to decrease of capacitive behavior as a smaller amount of charged particles can adsorb on the surface [99].

Slight positive ΔZ′ values were observed at the high-frequency range (f ≥ 10kHz). This result is most likely related to the decrease of oxygen vacancy concentration in LSCM lattice as pO_2 increases [113].

6.1.2 Influence of temperature on the single-cell impedance in the fuel cell mode

Differences of real part of impedance spectra, ΔZ′, for $La_{0.8}Sr_{0.2}Cr_{0.5}Mn_{0.5}O_{3-\delta}$| ScCeSZ|LSF in the temperature range of 700 to 850 °C revealed two distinct regions that were influenced by the change of temperature (Fig. 10).

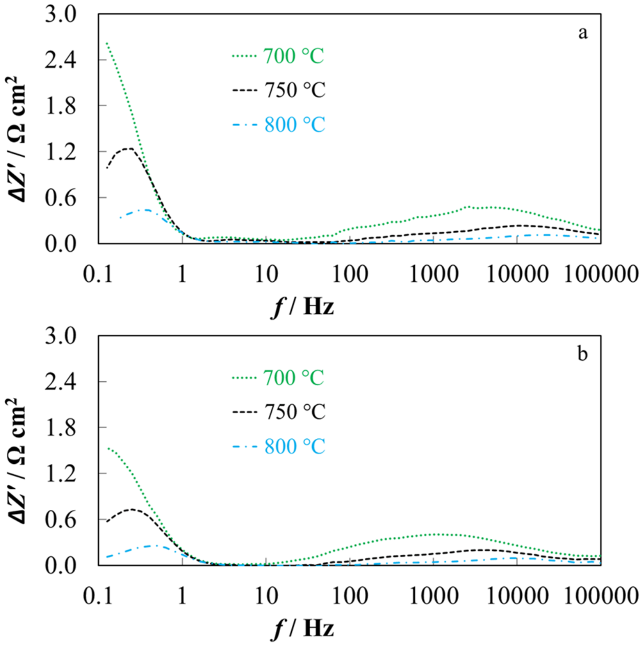

Figure 10. Differences of LSCM|ScCeSZ|LSF unit cell impedance component, ΔZ′, at OCV (a), and 0.8 V (b) unit cell potentials caused by the change of temperature (shown in the figure) compared to the impedance at 850 °C in gas environment with $pH_2 = 0.97$ and $pH_2O = 0.03$ atm.

High-frequency region of impedance change from 10 Hz to 100 kHz has been observed, which, according to literature data, can be attributed to changes in the oxygen vacancy concentration and ionic conductivity in LSCM as pO_2 changes [113].

The low-frequency region, where ΔZ′ increases drastically as temperature decreases, starts from around 2 Hz. According to literature data, this range is attributed to the rate limitations of gas-solid adsorption-desorption steps, which is confirmed by the large temperature dependence of the process [99,111].

The shift of frequency, where ΔZ′ is maximal, is probably related to the simultaneous change of resistive and capacitive behavior of materials. Also, the frequency range of maximal ΔZ′ if the temperature is varied is very similar to the frequency range of ΔZ′ maxima if pH_2 is varied, indicating that the limitations observed are probably caused by the characteristics of LSCM fuel electrode material.

6.1.3 Influence of cell potential on the single-cell impedance in the fuel cell mode

Similarly to the influence of temperature, the change of cell potential from OCV to 0.8 V at different temperatures revealed two regions of increased ΔZ′. As the decrease of potential increases the pO_2 in the fuel electrode compartment, the impedance is influenced similarly to the decrease of pH_2.

The high-frequency processes attributed to changes in the oxygen vacancy concentration and ionic conductivity in LSCM as pO_2 changes are influencing the impedance around 10 kHz [113].

The low-frequency processes are influencing ΔZ′ under 2 Hz and probably can be attributed to limitations of gas-solid adsorption-desorption steps [99, 111].

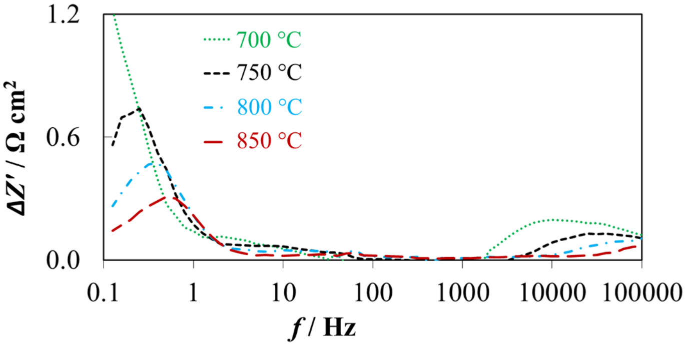

Figure 11. Differences of LSCM|ScCeSZ|LSF unit cell impedance component, ΔZ′, caused by the change of unit cell potential from OCV to 0.8 V at different temperatures (shown in the figure) in the gas environment with $pH_2 = 0.97$ and $pH_2O = 0.03$ atm.

6.1.4 Influence of water partial pressure in fuel gas on the single-cell impedance in the electrolysis mode

ΔZ′ graphs illustrating the change of real part of impedance caused by the change of water concentration in hydrogen water gas mixture at OCV and 1.5 V for some studied materials are shown in Figure 12. For the real part of impedance, the changes depend greatly on the chemical composition of the material as well as on the partial pressure of water in the fuel electrode compartment [110].

The ΔZ′, frequency-dependence for $La_{0.75}Sr_{0.25}Cr_{0.3}Mn_{0.5}Ni_{0.2}O_{3-\delta}$ (Fig. 12a) at the high-frequency range is significantly different compared to the data of other studied electrodes, most likely due to a higher concentration of redox activated d-elements, which change the oxidation state in the SOFC/SOEC regime (Mn, Ni) in the fuel environment [59]. According to previous results in the literature, the LSCMN system with $Cr_{0.3}Mn_{0.5}Ni_{0.2}$ B-site composition had a characteristic electrochemical behavior, showing an increase of activation energy, E_a, as pO_2 increases, while $Cr_{0.5}Mn_{0.3}Ni_{0.2}$ and $Cr_{0.5}Mn_{0.44}Ni_{0.06}$ demonstrated a decrease in E_a, thus, increase of electronic conductivity with an increase of pO_2 [59]. The increase of E_a is probably the reason why there were no changes in the high-frequency region for $La_{0.75}Sr_{0.25}Cr_{0.3}Mn_{0.5}Ni_{0.2}O_{3-\delta}$ based systems.

The reason for the increase in impedance at 25.1 kHz range (if pH_2O was decreased) for $(La_{0.8}Sr_{0.2})_{0.95}Cr_{0.49}Mn_{0.49}Ni_{0.02}O_{3-\delta}$ as well as 8 kHz range for $La_{0.8}Sr_{0.2}Cr_{0.5}Mn_{0.5}O_{3-\delta}$ was caused by the decrease of water concentration on the electrode surface, thus hindering the charge transfer processes, which are sensitive for adsorbed H_2O concentration, for oxide ion vacancy concentration and electrode potential [13]. Therefore, the characteristic ΔZ′ frequency values shifted from 25.1 to 15.8 kHz and from 8 to 2.5 kHz, i.e., to lower frequencies as 1.5 V cell potential was applied.

$La_{0.8}Sr_{0.2}Cr_{0.5}Mn_{0.5}O_{3-\delta}$ and $La_{0.75}Sr_{0.25}Cr_{0.3}Mn_{0.5}Ni_{0.2}O_{3-\delta}$ showed an increase in ΔZ′ at moderate (10-100 Hz) frequencies if pH_2O was decreased from 0.30 to 0.03 atm. According to the literature data, an increase in ΔZ′ at aforementioned frequency range can be attributed to hindered dissociative adsorption of reactive species in the electrolysis mode, especially at lower partial pressures of water [13].

The increase in the active component of impedance, ΔZ′, at lower frequencies than 1 Hz indicates the appearance of the gas conversion impedance at operating conditions (at 1.5 V) of electrolysis if low H_2O concentrations are used [112].

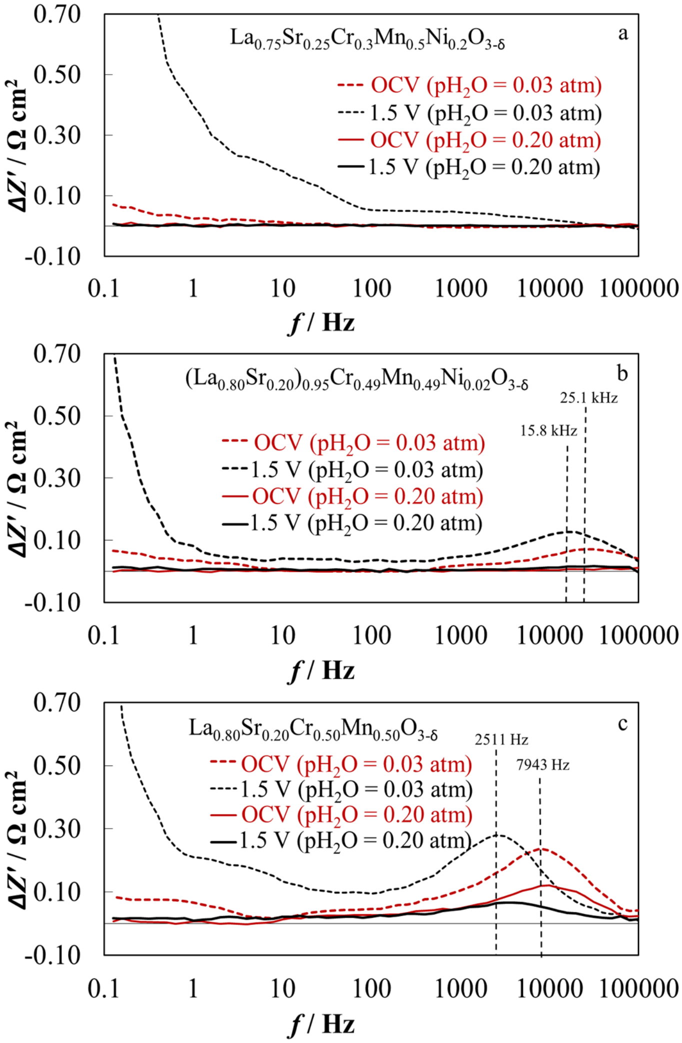

Figure 12. Differences of electrochemical cell impedance real part, ΔZ′, of LSCM|ScCeSZ|LSF (a), $(La_{0.8}Sr_{0.2})_{0.95}Cr_{0.49}Mn_{0.49}Ni_{0.02}O_{3-\delta}$|ScCeSZ|LSF (b) and $La_{0.8}Sr_{0.2}Cr_{0.5}Mn_{0.5}O_{3-\delta}$|ScCeSZ|LSF (c) cells (shown in the figure) at OCV and 1.5 V cell potentials at 850 °C, caused by shift of H_2O concentration in hydrogen electrode gas stream (shown in figure) compared to impedance in gas environment with pH_2 = 0.70 and pH_2O = 0.30 atm.

6.1.5 Influence of temperature on the single-cell impedance in the electrolysis mode

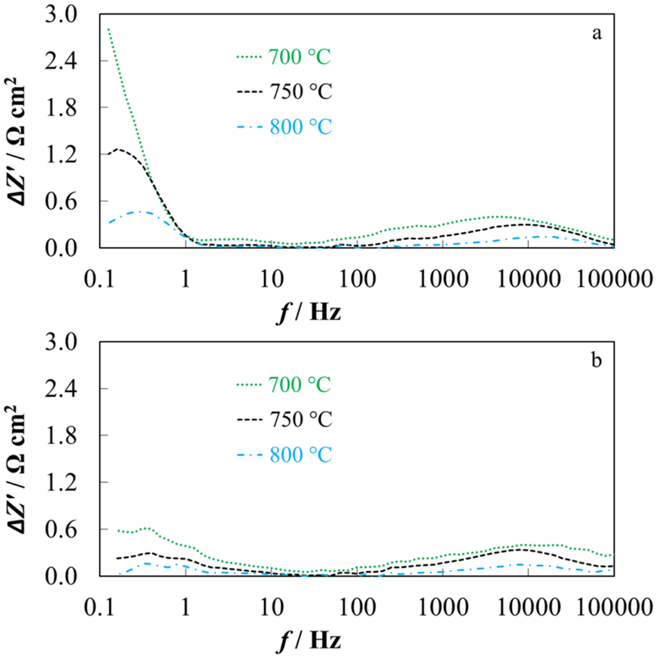

Figure 13. Differences of LSCM|ScCeSZ|LSF unit cell impedance real part component, ΔZ′, at OCV (a), and at 1.5 V (b) unit cell potentials caused by the change of temperature (shown in the figure) compared to the impedance at 850 °C in gas environment at $pH_2 = 0.70$ and $pH_2O = 0.30$ atm.

The dependence of Z′ on the temperature within the studied frequency range of $La_{0.8}Sr_{0.2}Cr_{0.5}Mn_{0.5}O_{3-\delta}$|ScCeSZ|LSF single-cell is very similar in fuel cell and electrolysis modes as confirmed by the differences of the real part of impedance, ΔZ′, spectra in the temperature range from 700 to 850 °C (Fig. 13).

The high-frequency region with positive ΔZ′, expanding from 100 Hz to 100 kHz, can be attributed to changes of oxygen vacancy concentration and ionic conductivity in LSCM if pO_2 changes [113].

ΔZ′ increases drastically with the decrease of temperature starting from 2 Hz to lower frequencies. According to literature data, this range is attributed to the kinetic limitations of gas-solid adsorption-desorption steps [99,111].

6.1.6 Influence of cell potential on the single-cell impedance in the electrolysis mode

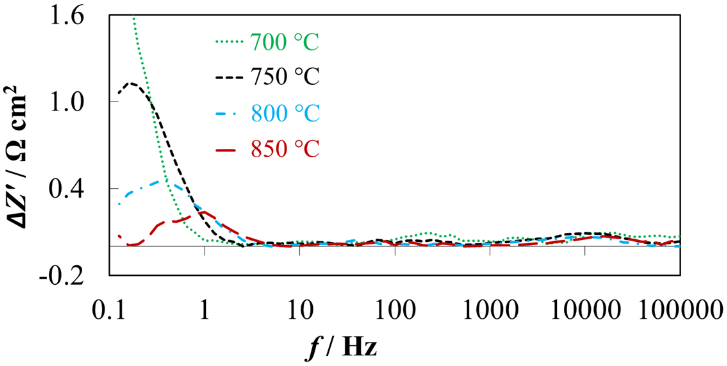

Figure 14. Differences of LSCM|ScCeSZ|LSF unit cell impedance component, ΔZ′, caused by the change of unit cell potential from OCV to 1.5 V at different temperatures (shown in the figure) in the gas environment at $pH_2 = 0.70$ and $pH_2O = 0.30$ atm.

The most noticeable difference between the ΔZ′ change caused by unit cell potential variation in fuel cell and electrolysis mode is seen in the high-frequency range. This difference is probably related to the already high pO_2 (compared to the fuel cell mode) in the studied system and very minimal changes in MIEC electrode material properties (Fig. 14). Therefore, the high-frequency range, which is attributed to the changes in the oxygen vacancy concentration and ionic conductivity in LSCM as pO_2 changes, is less influenced by the changes of cell potential on the studied single-cell [113].

At low-frequency region (2 Hz and lower), an increase of ΔZ′ appears if electrolyzer is under the load, which is very likely caused by limitations on gas-solid adsorption-desorption processes [99,111].

6.2 Optimization of porous electrolyte scaffolds

Two different approaches were combined to prepare electrodes with various porosities – (i) pre-sintering of electrolyte raw powder to change the particle size distribution and (ii) adding of a controlled amount of carbonaceous pore formers with different particle size distributions into the raw electrolyte paste [107].

The pre-sintering temperature of ScCeSZ raw powder was varied in the range from 1000 to 1300 °C (Fig. 15). The powder sintered at 1300 °C was chosen because of its relatively large particle size. Furthermore, spherical activated carbon particles (Strem 06-0100), fractions of lamellar graphite 1 (AE-028, TIMCAL), and lamellar graphite 2 (Fluka 78391) with particle sizes from 0 to 20 µm were used as the pore formers. Four distinctly different porous scaffolds were selected and characterized by many different types of obtained porous scaffolds (Fig. 16)

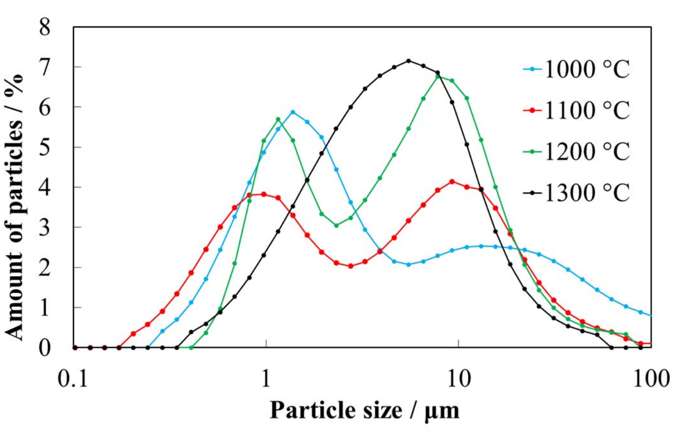

Figure 15. The particle size distribution of ScCeSZ complex oxide raw powders, pre-sintered at fixed temperatures ranging from 1000 to 1300 °C.

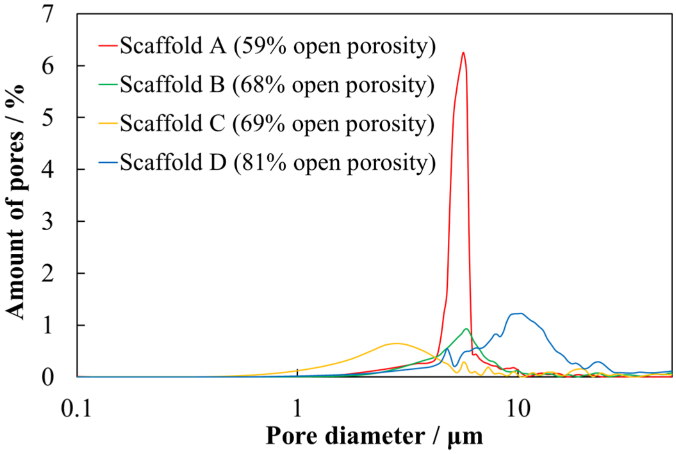

Figure 16. Hg porosimetry data for the pore size distribution of sintered porous scaffolds. Open porosities noted in the figure.

Porous scaffold A was prepared using unsintered ScCeSZ powder. Lamellar graphite 2 and activated carbon (Strem 06-0100) were used as pore formers, both of which 15% by mass were added to the screen-printing paste. As a result, a porous scaffold with 59% open porosity was prepared with 3–8 µm pores in diameter, having a maximum of pore size distribution at around 5.5 µm (Fig. 16).

Porous scaffold B was prepared from sintered (1300 °C) and unsintered ScCeSZ powder mixed in a 9:1 mass ratio. Lamellar graphite 2 and activated carbon were used as the pore formers. 15% by mass of both pore formers were added to the slurry, and a porous scaffold with 68% open porosity was obtained. Pore diameter varied from 3 to 8 µm, having a maximum around 6 µm.

Porous scaffold C was prepared from unsintered ScCeSZ powder and lamellar graphite 1, of which 35% by mass was added. Scaffold with 69% open porosity was prepared and the pore diameter varied from 1.2 to 5 µm, having a maximum around 2.6 µm.

Porous scaffold D was prepared from both sintered and unsintered ScCeSZ powder in a ratio of 9:1 by mass, and graphite 1 (35% by mass) was added. An electrolyte scaffold with 81% open porosity was obtained. Pore diameter varied from 4 to 19 µm, having a maximum of pore size distribution around 10 µm.

Selected porous scaffolds had different open-pore volumes as well as pore size distributions (Fig. 16 and 17). It is evident that total porosity, as well as the pore size distribution, is influenced by the properties of the pore former (comparison of A and C or B and D) and by the amount of pre-sintered electrolyte powder added into the screen-printing paste (comparison of A and B or C and D).

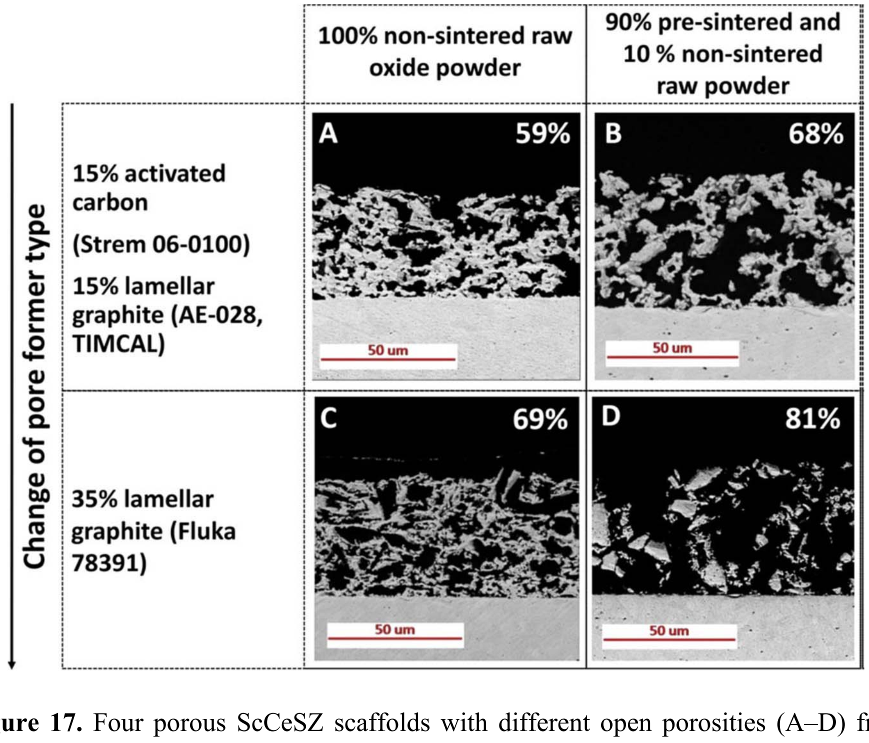

Figure 17. Four porous ScCeSZ scaffolds with different open porosities (A–D) from publication II [107].

The porosity of the scaffold was increased approximately 10 vol% by substituting 90 wt% of non-sintered electrolyte powder with pre-sintered oxide powder. The partial pre-sintering of ScCeSZ electrolyte powder led to the increase of the mean pore diameter when lamellar graphite 1 was used. However, this effect was weakly expressed in the case of the mixture of graphite 2 and activated carbon.

Irrespective of the pre-sintering of the electrolyte powder, the use of 35 wt% of lamellar graphite 1 instead of the mixture of 15 wt% graphite 2 and 15 wt% activated carbon led to an increase of porosity nearly 10 vol% [107].

6.3 Influence of electrode microstructure on the electrochemical performance of RSOC

6.3.1 Influence of electrolyte scaffold microstructure and loading of MIEC material on the electrochemical performance of RSOC

Electrochemical test results of cells using four different electrolyte scaffolds and different SFM loadings, given in Figure 18, indicate that there is a significant dependence of current density on the structural properties of the electrolyte scaffold used [107].

In the case of 10% of SFM loading (Fig. 13a), the highest current densities of 0.14 and 0.13 A cm^{-2} at 0.9 V (fuel cell mode) and –0.14 and –0.15 A cm^{-2} at 1.3 V (electrolysis mode) were measured for scaffolds A and C based cells, respectively at 800 °C. For scaffolds B and D based cells, the current densities were significantly lower, 0.03 and 0.05 A cm^{-2} at 0.9 V (fuel cell mode) and 0.06 A cm^{-2} at 1.3 V (electrolysis mode), respectively. The linear shape of i-E curves indicate characteristic ohmic limitations in the case of 10 wt% SFM loading (Figure 18a).

The current densities increased significantly, and characteristic diffusion-limited i-E curve with a weakly expressed current plateau appeared due to small water partial pressure from 1.3 V and higher cell voltages (electrolysis mode) after increasing SFM loading up to 20, and 30 wt% (Figures 18 b and c) [107]. Thus, the increase of SFM loading improved the conductive MIEC network in a porous electrode, which led to a decrease of ohmic limitations. On the other hand, the increase of SFM loading also decreased the porosity necessary for the transport of gaseous reactants and products of the electrochemical reaction. Further increase of SFM loading from 20 to 30 wt% had a minor influence on the electrochemical characteristics of the single-cell in case of scaffold D, but for scaffold C based cells, an increase of SFM loading led to a significant increase of current density in fuel cell mode. As shown in paper [76] about other composite electrode materials, infiltration already enables to achieve reasonable conductivities at quite low loadings. Depending on the electrolyte scaffold microstructure, the current density can be further enhanced by the increase of MIEC network in the porous scaffold.

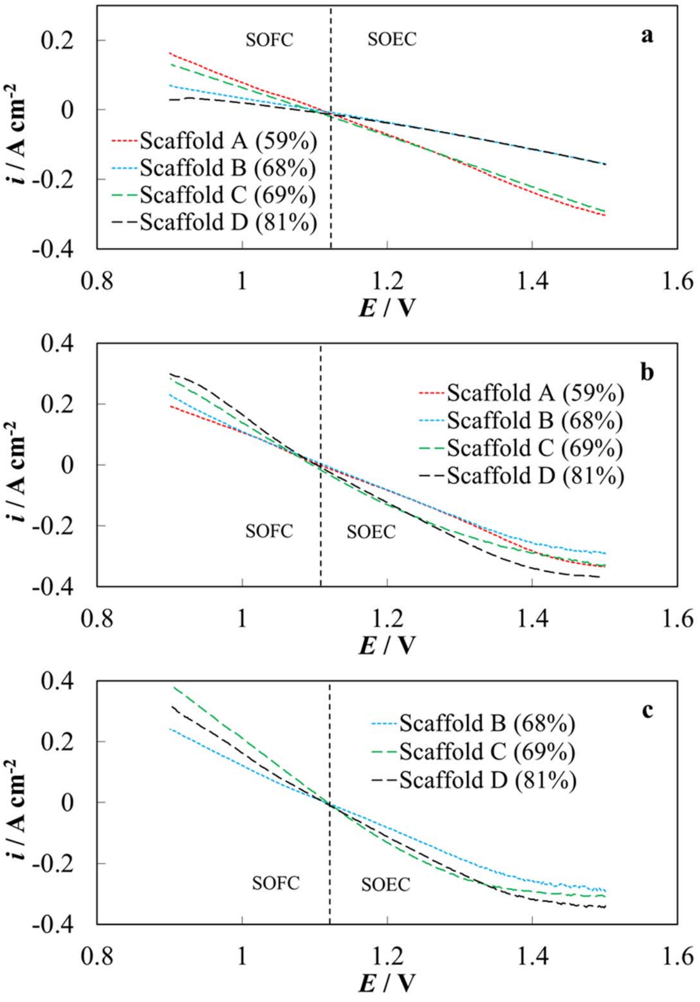

Figure 18. i-E curves for SFM|ScCeSZ|LSF single cells prepared using four porous electrolyte scaffolds in the fuel electrode side with SFM loadings of 10 (a), 20 (b), and 30 (c) wt.% (initial porosity of scaffolds noted in the figure). Measurements were carried out at 800 °C in fuel electrode gas inlet at $pH_2 = 0.97$ and $pH_2O = 0.03$ atm, using a potential sweep rate of 10 mV s^{-1}.

6.3.1.1 Influence of loading of SFM MIEC and porous electrolyte scaffold on the components of impedance

Data in figures 19 and 20 give a general overview of the influence of the electrolyte scaffold properties on series resistance, R_s, and polarization resistance, R_p, values as a function of SFM MIEC loading, cell potential, and temperature.

Series resistance, R_s, consists of the active resistance component of a dense electrolyte layer, of the resistances of the porous electrolyte scaffolds of both electrodes, and resistance of the MIEC matrix of both electrodes and therefore depends on temperature, on the microstructure of the electrolyte scaffold as well as on the amount of SFM deposited into the electrolyte matrix (Fig. 19).

A comparison of data in a, b, and c parts of Figure 19 confirms that the dependence of series resistance on the cell potential is minor owing to the fairly high conductivity of SFM [65]. However, larger changes are caused by electrolyte scaffold structure and by the amount of SFM deposited into those porous scaffolds. Series resistance values are higher for systems with 20 wt% of SFM loading compared with systems of 30 wt% SFM loading in the electrolyte matrix. R_s values of single-cells with lower loadings were not included as they were substantially higher.

As previously discussed, both R_s and R_p are influenced by many different parameters at the same time. The increase of the loading of MIEC material should increase the conductive MIEC network inside of the porous scaffold and, therefore, should decrease the series resistance of the systems studied. However, the R_s will decrease only as far as the infiltration will improve the electrical contact between active surface and current collector and between the electrolyte and MIEC material. A comparison of different electrolyte scaffolds with 30% of SFM loadings at different potentials reveals that the lowest R_s values are characteristic of scaffold D based electrode. Slightly higher (approx. 0.05 Ω cm^2) series resistance values were observed for electrolyte scaffold C based cells.

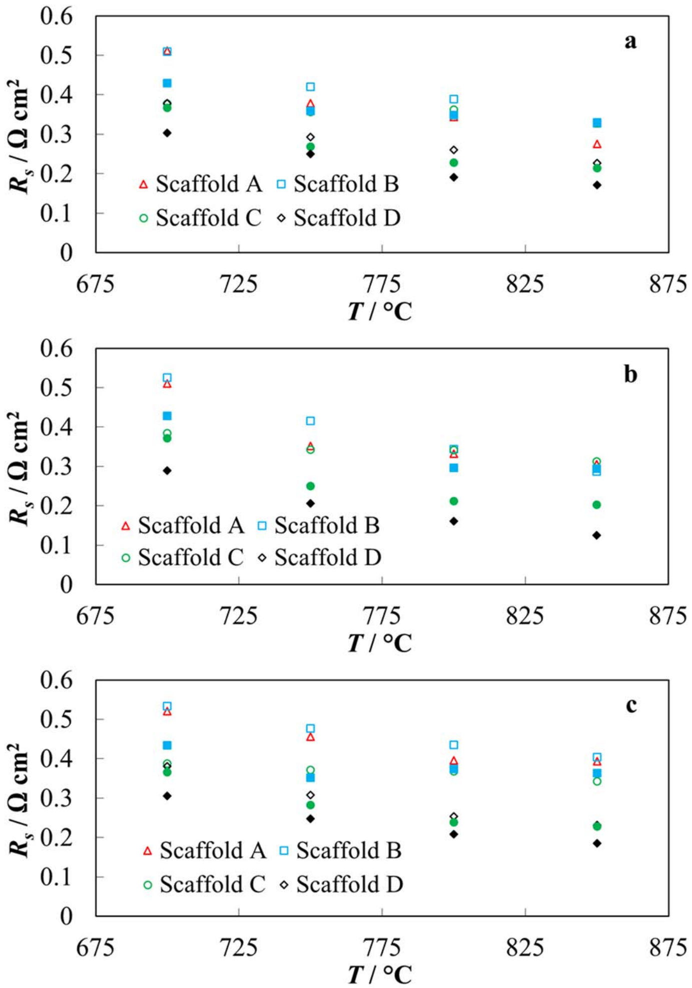

Figure 19. Dependence of ohmic resistance, R_s, of SFM|ScCeSZ|LSF single-cells on temperature, the porosity of the electrolyte scaffold, and on the loading of MIEC material. Loadings used were 20 (empty patterns) and 30 wt.% (filled patterns) (noted in figure). Measurements were carried out at 800 °C in fuel electrode gas inlet at pH_2 = 0.97 and pH_2O = 0.03 atm at OCV (a), 0.9 V (b), and 1.3 V (c).

Dependence of R_p on the microstructure of the electrolyte scaffold and amount of SFM in the porous scaffold is much more complicated compared to the dependencies of R_s.

In the fuel cell regime, the lowest R_p values were detected for scaffold C based cells with 20 and 30 wt% of SFM loadings (Fig. 20a). Scaffold C with 20 wt% SFM loading demonstrated significantly lower R_p values compared to 30 wt% of SFM loading at lower temperatures due to the improved transport porosity of the 20 wt% of SFM system. This is also the reason why scaffolds with smaller open pore volume acquire higher R_p values at higher SFM loading.

At electrolysis mode (Figure 20c), the dependence of R_p becomes even more dependent on scaffold microstructure (transport porosity) and SFM loading because the speed of mass transport is more affected on the microstructure in the case of H_2O and CO_2 molecules (slower diffusion compared to H_2) [96,114]. Furthermore, the local temperature gradient across the electrode due to the endothermic nature of electrolysis could further decrease the speed of diffusion of the molecules [115]. In the current study, the lowest R_p values (electrolysis mode) at low water partial pressures (0.03 atm) were more than 100% higher compared to R_p values measured at fuel cell mode.

In the case of C and D scaffolds with SFM loading of 30 wt%, the R_p increases for C and D scaffolds with the increase of temperature starting from 800 °C and 750 °C, respectively. This phenomenon might be caused by the formation of undesirable phases because of too high oxygen partial pressures in the surface layer of these electrodes. This speculation is also supported by the fact that there is also a slight relative increase of R_s value at higher temperatures in the electrolysis mode in the case of scaffold C, which has the highest increase of R_p at elevated temperatures. This relative increase of R_s with temperature could be only caused by the changes in properties of SFM structure. For a deeper understanding, these electrodes should be studied using high-temperature X-ray diffraction (HT-XRD) and simultaneous electrochemical impedance spectroscopy (EIS) methods at operating conditions. However, based on results available from preliminary electrochemical characterization, the lowest R_p values were obtained if scaffolds C and D were used with 20 and 30 wt% of SFM [107].

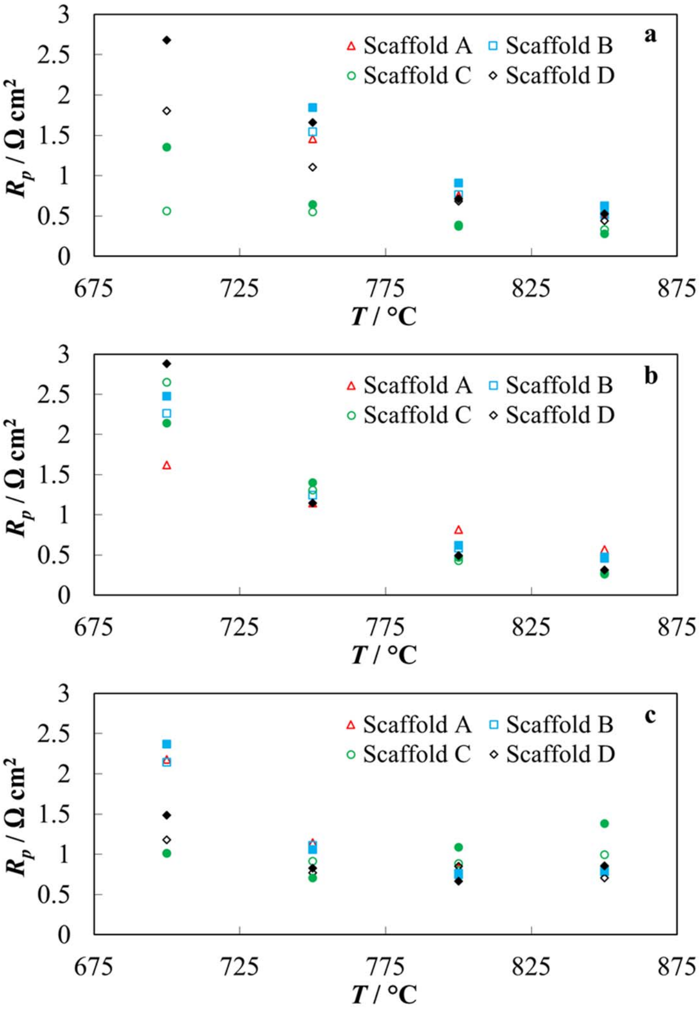

Figure 20. Dependence of polarization resistance of SFM|ScCeSZ|LSF single cells, R_p, on temperature, on the porosity of electrolyte scaffold, and on the loading of MIEC into scaffolds. Loadings used were 20 (empty patterns) and 30 wt.% (filled patterns) (noted in the figure), respectively. Measurements were carried out at 800 °C in fuel electrode gas inlet at pH_2 = 0.97 and pH_2O = 0.03 atm and at OCV (a), 0.9 V (b), and 1.3 V (c), respectively.

Figure 21 shows impedance data for single cells prepared using scaffolds C and D (noted in the figure), which showed the best results in the initial characterization of scaffolds.

Noticeably, the R_p depends only very slightly on the type of scaffold and SFM loading. However, more remarkable changes can be seen in series resistance values. Lowest series resistances were measured for the electrodes made using scaffold D and 30 wt% of SFM loading, and R_p increased slightly if scaffold C was used instead. An additional increase in series resistance occurred if SFM loading was decreased from 30 to 20 wt% due to the insufficient MIEC material network for ionic transport.

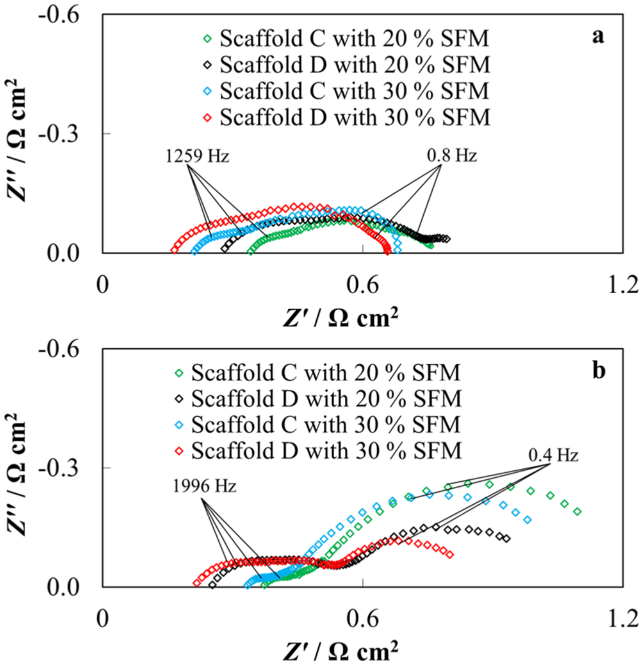

Figure 21. Nyquist plots of SFM|ScCeSZ|LSF single cells prepared using porous electrolyte scaffolds C and D in the fuel electrode side with various SFM loadings (noted in the figure). Measurements were carried out at 0.9 V (a), 1.3 V (b) and at 800 °C in fuel electrode gas inlet at $pH_2 = 0.97$ and $pH_2O = 0.03$ atm.

Furthermore, significant differences between C and D scaffold-based cells are visible in the electrolysis mode at 800 °C. Cells based on scaffold D have lower series resistances compared to single cells based on scaffold C, which might be caused by less fragmented nature of MIEC material in bigger pores (scaffold D) compared with scaffold with smaller mean pore diameter. In the case of both scaffolds, the increase of SFM loading decreases the series resistance as well as the charge transfer resistance.

The high-frequency impedance spectrum arc, associated with dissociative adsorption of the reactive species or mass transport of oxide ions in MIEC, is wider in the case of scaffold D, indicating the existence of lower concentration of active centers for the adsorption [13]. As scaffold C has smaller open pore volume, the smaller mean size of the pores, and thus, larger specific surface area, it is highly likely that this is the reason for the higher specific surface area of the electrode after the infiltration with the MIEC material.

Low-frequency impedance spectrum arc, which could be associated with mass transport limitations in pores at electrolysis mode (Fig. 21b), depends significantly on the electrolyte scaffold type used. At both SFM loadings, the scaffold D has a smaller low-frequency arc compared to scaffold C based cells, which has smaller porosity. In a comparison of electrodes with different SFM loadings, it is evident that higher SFM loading leads to smaller series and charge-transfer resistance values (more active centers connected with a sufficient amount of conductive matrix) [107].

6.3.2 Co-effect of MIEC conductivity and electrolyte scaffold porosity on the electrochemical performance of RSOC

Data in figure 22 shows the influence of the loading of SFM (550 S/cm at 780 °C in the air) and LSCMN (38 S/cm at 900 °C in the air) in electrolyte scaffold D (~81% porosity) on unit cell complex impedance. Based on the initial characterization data for electrodes with SFM and the low conductivity of the LSCMN, scaffold D was chosen for the preparation of LSCMN composite electrodes, because it enabled very high loading of the MIEC material.

For SFM, the increase of loading from 30 to 50 wt% of MIEC material did not improve the performance of the single cells. In the case of LSCMN, the optimal loading of MIEC material was higher compared to SFM due to the lower conductivity of the LSCMN material. Therefore, at least 50 wt% of MIEC material was necessary to achieve reasonable R_s and R_p values. As a result, an increase of MIEC from 30 to 50 wt% loading led to a considerable decrease in cell total resistance.

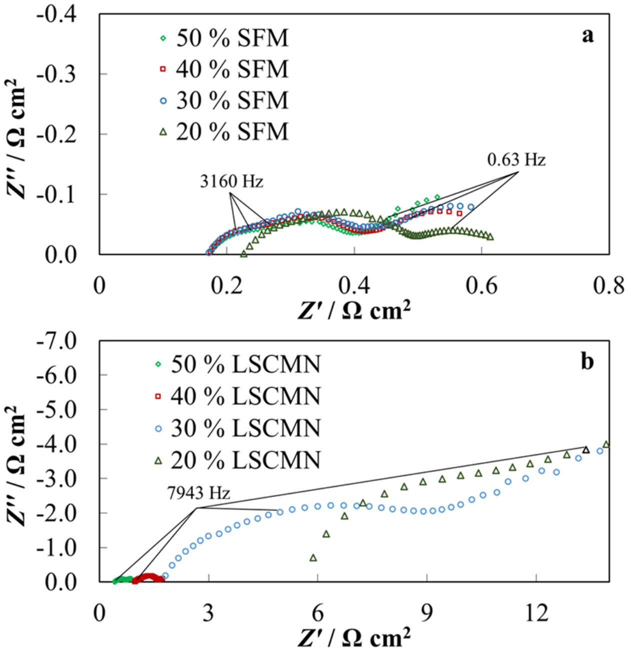

Figure 22. Nyquist plots of SFM|ScCeSZ|LSF (a) and LSCMN|ScCeSZ|LSF (b) single cells prepared using porous electrolyte scaffold D impregnated with 20 to 50 wt% MIEC material in the fuel electrode side (noted in the figure). Measurements were carried out at OCV and at 850 °C in fuel electrode gas inlet at $pH_2 = 0.97$ and $pH_2O = 0.03$ atm.

To conclude, it is evident that the optimal loading of MIEC depends on the type of material and is always accompanied by the decrease of transport porosity as the loading of MIEC increases. Therefore, an optimal ratio of two parameters yields the best performance of the electrode.

6.4 Influence of the chemical composition of MIEC materials on the electrochemical performance of cells in the fuel cell mode

Fig. 23 shows Nyquist plots for all of the studied materials at OCV (a) and at 0.9 V (b) (fuel cell mode) at 800 °C. Studied materials include LSCM with various A- and B-site modifications, as well as SFM, for its novelty and potentially better conductivity in SOC working conditions. As previously mentioned, perovskites enable a very diverse set of properties through the crystal lattice with many different cations. Therefore, the properties of the specific compositions are expected to be a combination of many simultaneous parameters.

Unmodified $La_{0.8}Sr_{0.2}Cr_{0.5}Mn_{0.5}O_{3-\delta}$ showed the highest polarization resistance, R_p, values, especially at low frequencies, which, according to other authors, is related to the kinetic limitations of the gas-solid adsorption-desorption [99,111]. It is evident that modifications generally increased the catalytic properties of LSCM depending on the doping and A-site deficiency of the materials. Unlike other compositions, 20 mol% A-site deficient $(La_{0.8}Sr_{0.2})_{0.80}Cr_{0.49}Mn_{0.49}Ni_{0.02}O_{3-\delta}$ had very similar (at OCV) or even higher (at 0.9 V) R_p value than that of pure $La_{0.8}Sr_{0.2}Cr_{0.5}Mn_{0.5}O_{3-\delta}$. In general, R_s and R_p were both largely affected by the changes of A- and B-site composition (Fig. 23). The increase in A-site deficiency led to charge compensation phenomena through the simultaneous oxidation of B-site elements as well as the creation of oxide ion vacancies through the release of oxygen from the crystal lattice [116]. The increase in the concentration of oxide ion vacancies led to an increase in unit cell volume and a decrease in electronic conductivity. Although an increase of charge of B-site cations (the compensation effect) can also lead to a decrease of M-O-M length and the improved polaron hopping (higher conductivity), it did not seem to be a dominating effect for materials studied in current work [117]. Decreased electronic conductivity was most likely the reason for the increase of the total polarization resistance for cells with 5 to 20 mol% A-site deficiency because the number of active sites at MIEC also depends on the electronic conductivity of MIEC material. As a result, the high-frequency arc, which originates from the mass transport of oxide ions in MIEC, was greatly influenced by the chemical composition of materials studied [113].

However, some authors have used A-site deficiency to increase the catalytic activity either through the improved exsolution of B-site catalysts (Ni, Cu, etc.) or to suppress Sr segregation onto the surface of MIEC material [118]. So, it is also possible that a decrease in R_p is related to the more effective segregation of B-site cations with lower segregation energies onto the surface of LSCM (Ni, MnO), which can lead to the decrease of low-frequency impedance [109]. According to the results of other authors, low-frequency semi-circle is mainly related to the kinetics of gas-solid adsorption-desorption steps, thus results in this work confirm the improved catalytic properties for most of the studied materials [99,111].

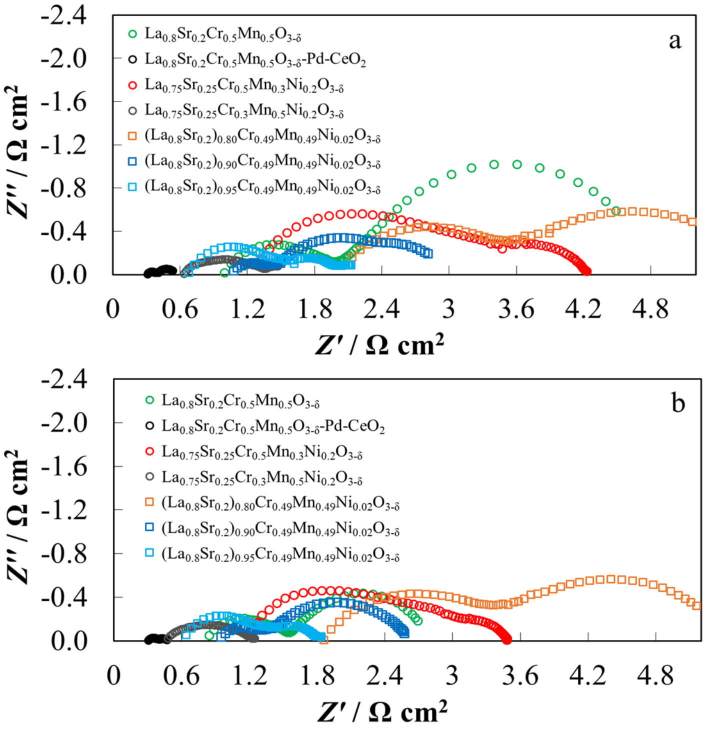

Figure 23. Nyquist plots at OCV (a) and at 0.9 V (b) unit cell potentials at 800 °C for studied unit cells (given in Figure) showing unit cell series and polarization resistances of different LSCMN A- and B-site composition as well as Pd and CeO_2 infiltrated LSCM in gas environment at $pH_2 = 0.97$ and $pH_2O = 0.03$ atm.

Interesting results were obtained for B-site modifications of LSCM as well. R_p increased about three times when concentrations of chromium and manganese were exchanged ($Cr_{0.5}Mn_{0.3}Ni_{0.2}$ vs. $Cr_{0.3}Mn_{0.5}Ni_{0.2}$). Most likely, this effect can be explained by the changes in defect equilibrium controlling electronic transport. This is mostly influenced by the changes in the valence state of Mn as Cr is shown to keep its valence under working conditions (Fig. 23) [116,119]. On the other hand, changes of R_p cannot only be explained by the changes in the conductivity of the material (caused by the change of Mn valence in the LSCM lattice) as LSCM with 2 mol% of Ni in B-site consisted of 49 mol% of Cr in B-site and this material still had lower polarization resistance. Jardiel et al. [59] showed that an increase of Ni concentration in B-site from 6 to 20 mol% decreased conductivity in oxygen and 5% H_2/95% Ar atmospheres for LSCM-based materials. However, conductivity was still better than in the case of unmodified LSCM material, showing the importance of the optimal amount of Ni in oxide structure. Best area-specific resistances were achieved for

$La_{0.8}Sr_{0.2}Cr_{0.5}Mn_{0.5}O_{3-\delta}$-Pd-$CeO_2$ showing good catalytic properties of Pd and CeO_2 catalysts.

Under polarization, most materials show some decrease of R_p by the change of activation energy according to the Butler-Volmer equation. Some additional decrease of R_p at 0.9 V might come from the increase in pO_2 at the anode in fuel cell operating conditions. The increase of pO_2 leads to an increase of electronic conductivity and also to the increase in the number of active sites in the electrode, and thus, to the decrease of R_s and R_p, respectively [9].

To conclude, our results show the complex nature of the MIEC electrodes in the fuel cell mode, where the role of ionic- and electronic conductive properties (dependence on pO_2), as well as surface catalytic behavior, play an important role.

6.5 Influence of the chemical composition of MIEC materials on the electrochemical performance of cells in the electrolysis mode

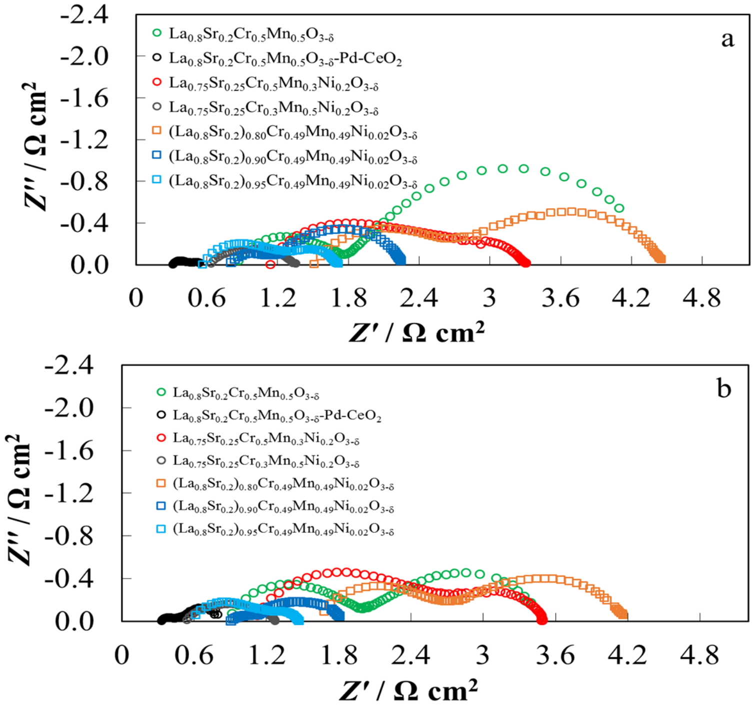

Figure 24. Nyquist plots at OCV (a) and at 1.5 V (b) unit cell potentials at 800 °C for studied unit cells showing changes of unit cell series and polarization resistances induced by the change of LSCMN A- and B-site composition in a gas environment at $pH_2 = 0.80$ and at $pH_2O = 0.20$ atm.

Similarly to fuel cell mode, the A- and B-site modifications, as well as infiltration of catalyst nanoparticles into the electrode, influenced the series and polarization resistances of cells in the electrolysis mode. Furthermore, trends were similar to fuel cell mode (Fig. 24).

Studied materials showed clear trends that R_s increased when A-site deficiency increased. There are many simultaneous processes that influence such behavior, for example, the changes in oxide vacancy concentration or intensified segregation of B-site cations and, therefore, the possible formation of non-functional phases due to the changes in B-site cation charge [118]. The results of the current work are in good accordance with the literature data, where it has been shown that the conductivity of $La_{0.75}Sr_{0.25}Cr_{0.5}Mn_{0.3}Ni_{0.2}O_{3-\delta}$ is lower compared to $La_{0.75}Sr_{0.25}Cr_{0.3}Mn_{0.5}Ni_{0.2}O_{3-\delta}$ [59].

Variations in R_p values were also large. One of the reasons was the increase in the concentration of oxide ion vacancies, which led to an increased unit cell volume and decreased electronic conductivity. Decreased electronic conductivity is most likely also the reason for the increased polarization resistance because the electrochemically active surface area of MIEC depends on the electronic conductivity of MIEC material. It is also possible that the exsolution of metal catalysts is influenced by higher pO_2 (compared to fuel cell mode), resulting in characteristic changes of polarization resistances.

There was no systematic change in the impedance high-frequency semicircle, which is generally assigned to charge transfer reaction or electrical double layer charging at the grain boundaries [112,120]. In general, electrodes with Pd and CeO_2 infiltrated into the LSCM showed the lowest complex resistance due to the highly catalytically active surface area, compared to the bare LSCM (Fig. 24).

Higher adsorption-desorption resistance of electrodes with higher A-site deficiency can indicate instability and formation of non-functional phases in the materials studied [44]. For B-site modifications, a very high R_p for $La_{0.75}Sr_{0.25}Cr_{0.5}Mn_{0.3}Ni_{0.2}O_{3-\delta}$ is probably caused by high R_s values of the material studied. Poor conductivity of $La_{0.75}Sr_{0.25}Cr_{0.5}Mn_{0.3}Ni_{0.2}O_{3-\delta}$ compared to other compositions was reproducible through several experiments and according to literature data, is partly generated by the higher concentration of Cr, which prefers to keep the six-fold coordination and therefore, is not prone to change its valence, oppositely from Mn [116]. At the same time, the comparison of $(La_{0.8}Sr_{0.2})_{0.95}Cr_{0.49}Mn_{0.49}Ni_{0.02}O_{3-\delta}$ with $La_{0.75}Sr_{0.25}Cr_{0.5}Mn_{0.3}Ni_{0.2}O_{3-\delta}$, which have similar Cr concentrations, have very different R_p values. Therefore, many different processes influence the electrochemical behavior of these materials simultaneously.

In general, all studied compositions of LSCMN materials behaved differently under electrolysis conditions. Changes in complex impedance caused by gas composition and cell potentials appeared at different frequency ranges. Relative changes at the high and mid-frequency region were larger for $La_{0.8}Sr_{0.2}Cr_{0.5}Mn_{0.5}O_{3-\delta}$ than for $(La_{0.8}Sr_{0.2})_{0.95}Cr_{0.49}Mn_{0.49}Ni_{0.02}O_{3-\delta}$ and

$La_{0.75}Sr_{0.25}Cr_{0.3}Mn_{0.5}Ni_{0.2}O_{3-\delta}$, indicating better catalytic and conductive properties of material containing Ni catalysts. Still, an additional detailed systematic analysis with spectroscopic information about the valences of B-site components would be necessary to understand the conductivity behavior of studied materials.

6.6 Electrochemical performance of CeO_2 and Pd infiltrated $La_{0.8}Sr_{0.2}Cr_{0.5}Mn_{0.5}O_{3-\delta}$ electrode in co-electrolysis mode

From all of the studied materials, Pd and CeO_2 activated LSCM showed the best performance in fuel cell and electrolysis modes. This material was studied in the co-electrolysis mode of H_2O and CO_2. High-temperature co-electrolysis is a complex set of electrochemical reactions and thermodynamic equilibrium. Furthermore, the coupling of those reactions makes the determination of rate-limiting steps and the extent of each reaction quite complicated [121].

Data in figure 25a show the i-E curves during the co-electrolysis and fuel cell operation modes at several working temperatures. Relatively high current density values were recorded in both working regimes. Current density values increased with the working temperature for the fuel gas inlet at $pH_2O=0.03$, $pH_2=0.485$, and $pCO_2=0.485$ atm, respectively. However, current density values were somewhat lower compared with similar single-cell compositions prepared using the infiltration method by Yoon et al. [105]. Possible reasons for differences include the application of different electrolytes, variation in the thickness of the electrolyte, the microstructure of the porous electrolyte scaffold, and applied inlet gas feeding conditions.

In general, no hysteresis in i-E curves was observed, but some non-linearity of the i-E curves appeared at lower temperatures, indicating the low rate of the limiting faradic processes in SOEC and SOFC modes. The corresponding open circuit voltage values were 1.03 V, 1.01 V, 1.00 V, and 0.98 V at 650°C, 700°C, 750°C and 800°C, respectively, being in an agreement with the calculated ones.

Figure 25 b and c show the Nyquist plots for the single-cell analyzed in a fuel cell (E~OCV-0.3 V) and co-electrolysis (E~OCV+0.3 V) modes at various temperatures. Series resistance values, R_s, were slightly (~7 %) higher in co-electrolysis mode, being 0.9, 0.63, 0.44 and 0.34 Ω cm^2 at 650 °C, 700 °C, 750 °C and 800 °C, respectively. Changes in oxygen stoichiometry in LSCM cathode resulting in lower electron conductivity could explain the slightly higher R_s values in co-electrolysis mode.

The polarization resistance, R_p, was similar for both operation modes at all temperatures, having values of 0.75, 0.40, 0.17 and 0.14 Ω cm^2 at 650°C, 700°C, 750°C, and 800°C, respectively. However, the shape of the Nyquist curve varied somewhat, indicating a change in limiting processes at different temperatures.

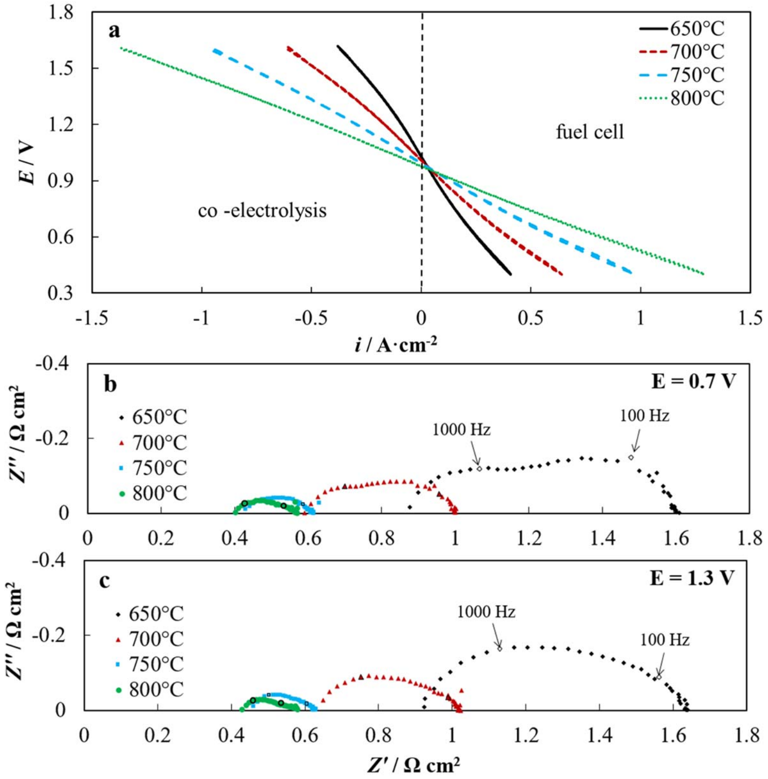

Figure 25. i-E curves measured at potential scan rate 20 mV s^{-1} (a) and Nyquist plots measured at fuel cell (b) and co-electrolysis (c) modes at different temperatures (noted in the Figure) in fuel electrode gas inlet at $pH_2O = 0.03$, and at $pH_2 = pCO_2 = 0.485$ atm, respectively.

Figure 26 shows a comparison of the single-cell electrochemical performance in steam (a) and co-electrolysis (b) operation modes at different temperatures using various fuel electrode gas compositions. Characteristic diffusion-limitation plateau appears at low water partial pressures during steam electrolysis at higher cell voltages. There are still big disputes between different working groups up until the writing of the current thesis concerning the CO_2 electrolysis during co-electrolysis. Kim-Lohsoontorn [122] and Stoots et al. [123] showed that SOC performance does not depend on the addition of CO_2, and part of the species was reduced due to thermodynamic equilibrium of reverse water-gas shift (RWGS) reaction. Inversely, co-electrolysis performance observed Graves et al. [124] was something between individual electrolysis of CO_2 and steam, and therefore authors concluded that part of the CO_2 was reduced through electrochemical reaction as well.

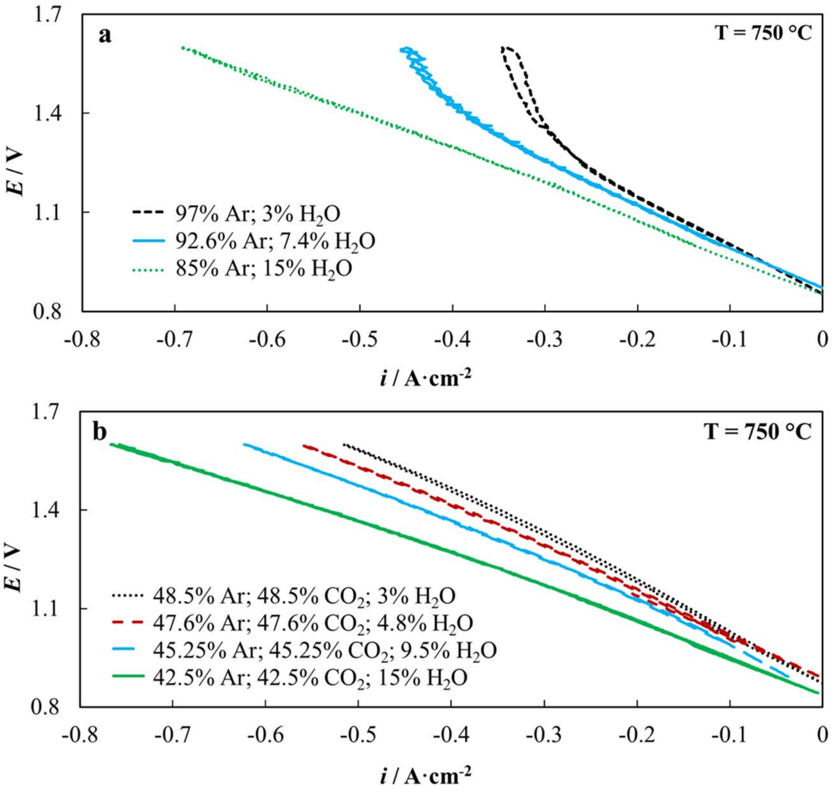

Figure 26. i-E curves for steam (a) and co-electrolysis (b) modes at 750 °C for LSCM-Pd-CeO_2|ScSZ|LSF at different fuel electrode gas inlets (noted in the Figure).

Current results indicate that some of the CO_2 has to be reduced electrochemically at low water partial pressure (0.03 atm) because characteristic diffusion limitation plateau (very likely caused by the difficulties of H2O diffusion to active centers) disappears during co-electrolysis, possibly due to the electrochemical reduction of CO_2 (Fig. 26b).

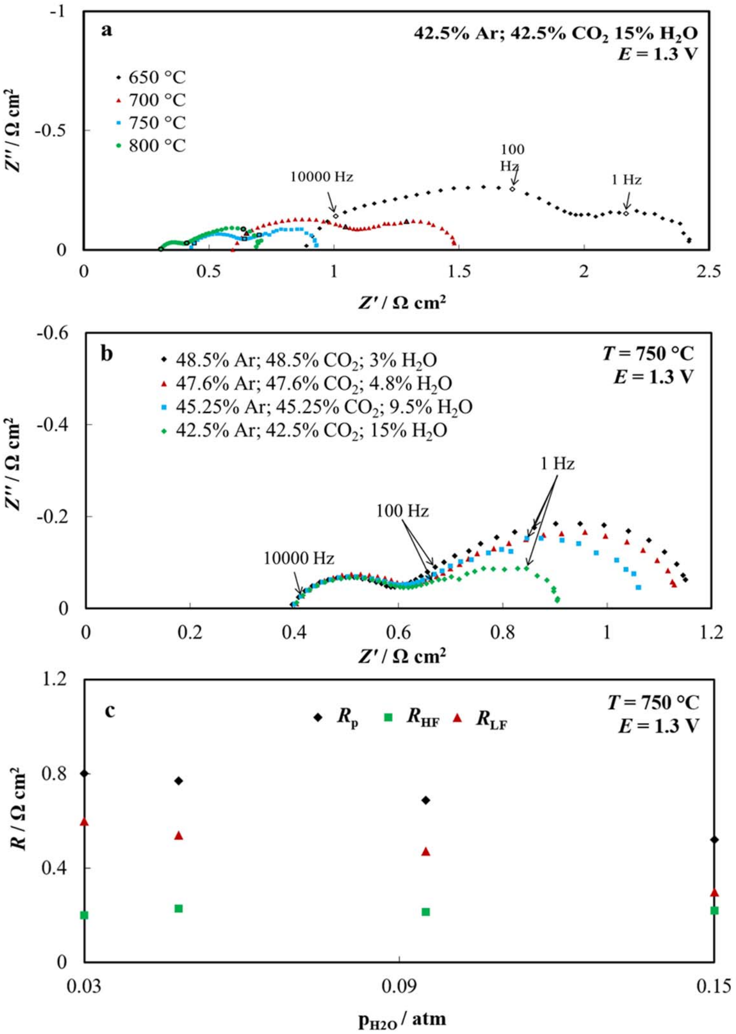

Figure 27. Nyquist plots at fixed cell potential of 1.3 V at different temperatures (noted in the Figure) (a), at 750 °C at fixed cell potential of 1.3 V and different fuel electrode gas inlets (noted in the Figure) (b) and dependence of total (R_p), high-frequency semi-circle (HF) and low-frequency semi-circle (LF) resistance values on H_2O partial pressure in the cathode gas (c).

The resistance of high-frequency semi-circle did not depend on the fuel electrode gas composition, having a value of 0.23 Ω cm^2 (Fig. 27b); therefore, the charge transfer reaction rate, electrical double layer charging at grain boundary interfaces, or three-phase boundary did not depend on the fuel electrode gas composition.

As a result, at 1.3 V, most of the change in polarization resistance arose from the low-frequency semi-circle, which was sensitive to water partial pressure. The initial resistance of 0.60 Ω cm^2 decreased to 0.30 Ω cm^2 when the steam partial pressure increased from 0.03 to 0.15 atm, indicating improved diffusion and dissociative adsorption of reactive species [13].

From Figure 28, it is evident that the production of hydrogen was dominant at lower temperatures, as expected because of the lower activation energy of the steam reduction reaction. Furthermore, the final outlet gas composition was also influenced by the water-gas shift (WGS) reaction:

$$CO + H_2O = CO_2 + H_2 \; (\Delta H_{800°C} = -36.82 \text{ kJ/mol}) \quad (11)$$

At lower temperatures, WGS reaction shifts towards the formation of CO_2 and H_2; thus, hindering the formation of CO in the electrochemical reaction, but some is still present due to the chemical equilibrium. At higher temperatures (≥816 °C), WGS shifts to the formation of CO and H_2O. Therefore, partial pressure of CO increases due to both faster kinetics of electrochemical CO_2 reduction at higher temperatures and due to the chemical equilibrium of WGS. The production of CO also increases with the cell potential; however, current work does not aim to differentiate between the CO created through electrochemical or chemical reduction of CO_2. Therefore, at certain cell potential, some of the generated CO originates from the electrochemical and some from the chemical reaction [121]. Surely, this is an interesting topic for the future and should be studied in more detail.

To summarize, depending on the desired produced synthesis gas H_2/CO ratio, one needs to choose the suitable fuel electrode inlet gas concentrations and temperature. As shown for the Ni-YSZ electrode, the syngas quality can be easily adjusted to the desired H_2/CO ratio through the choice of correct thermodynamic operating conditions of the cell as well as of the fuel electrode compartment gas composition [125].

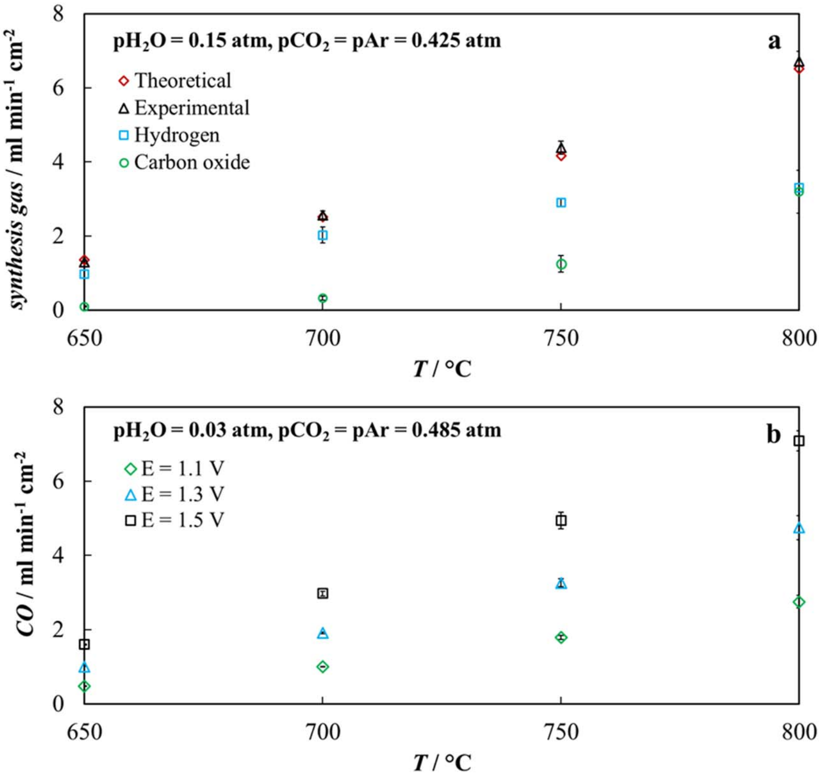

Figure 28. Synthesis gas production vs. cell temperature data at 1.5 V and at pH_2O = 0.15 atm, pCO_2 = pAr = 0.425 atm (a), CO production vs. cell potentials at different temperatures for hydrogen electrode gas inlet pH_2O = 0.03 atm, pCO_2 = pAr = 0.485 atm (b).

7. SUMMARY

$(La_{1-x}Sr_x)_yCr_{0.5-z}Mn_{0.5-w}Ni_{z+w}O_{3-\delta}$, CeO_2 and Pd infiltrated $La_{0.8}Sr_{0.2}Cr_{0.5}Mn_{0.5}O_{3-\delta}$, and $Sr_xFe_{1-y}Mo_yO_{6-\delta}$ mixed ionic electronic conductive fuel electrode materials were prepared and studied as potential reversible solid oxide fuel cell electrode materials.

In the first part of the thesis, the influence of test condition variation on the complex electrochemical impedance response of the system was visualized using the analysis of differences in impedance spectra (ADIS). The results of current work revealed that the most notable changes were induced around 0.5 Hz frequency range, and attributed to gas-solid adsorption-desorption processes rather than induced by gas conversion impedance. The substitution of Mn with Ni in the B-site of LSCM significantly increased the electronic conductivity of the MIEC material and improved the electrode properties at a mid- and low-frequency region associated with adsorption and dissociation processes of H_2. Variation of pO_2 in the oxygen electrode compartment led to a small variation in a total impedance of the studied single cells, but processes in cathode were not dominantly limiting in $(La_{1-x}Sr_x)_yCr_{0.5-z}Mn_{0.5-w}Ni_{z+w}O_{3-\delta}$|CeScSZ|LSF-based systems analyzed in this work.

In the second part of the thesis, the influence of the electrolyte scaffold structure on the electrochemical performance was studied. It was demonstrated that the pre-calcination and milling process of ScCeSZ electrolyte powder increased the average pore sizes as well as the overall porosity of the electrolyte scaffolds by about 10 vol. %. However, due to the use of pre-calcined electrolyte powder with the increased particle sizes, at lower MIEC loadings, the specific surface area of electrolyte scaffolds and catalytic activity decreased. As a result, at low MIEC loadings, scaffolds prepared from non-pre-sintered ScCeSZ powder showed better electrochemical performance. However, at higher MIEC loadings, best results were obtained for porous scaffolds based cells with higher pore sizes and the open-pore volume due to the optimal ratio between increased amount of conductive MIEC network and sufficient transport porosity for reactants.

In the third part of current work, the influence of the chemical composition of the MIEC electrode on the electrochemical performance of reversible solid oxide fuel cells at different operating regimes was studied. Modifications of the MIEC chemical composition revealed a remarkable influence on the electrochemical behavior of the solid oxide single cells. Most notably, polarization resistance of $La_{0.75}Sr_{0.25}Cr_{0.3}Mn_{0.5}Ni_{0.2}O_{3-\delta}$ material was about three times smaller than that for a very similar $La_{0.75}Sr_{0.25}Cr_{0.5}Mn_{0.3}Ni_{0.2}O_{3-\delta}$ material. Such difference was explained by an effect of defect equilibrium controlling the electronic transport, which was influenced by the change in the valence state of Mn as Cr has been shown to keep a stable valence under the working conditions. At the same time, $(La_{0.8}Sr_{0.2})_{0.95}Cr_{0.49}Mn_{0.49}Ni_{0.02}O_{3-\delta}$, a material with moderate A-site deficiency and similar concentration of Cr in the B-site as

$La_{0.75}Sr_{0.25}Cr_{0.5}Mn_{0.3}Ni_{0.2}O_{3-\delta}$, showed over two times smaller polarization resistance. Thus, change in Mn valence, nor the concentration of Ni in the B-site could not explain the changes in the electrochemical behavior of materials. Generally, the results of this work demonstrated the complex nature of the MIEC electrodes upon the modification in chemical composition, where the ionic- and electronic conductive properties (dependence on pO_2), as well as surface catalytic behavior, played an important role.

From all of the studied materials, Pd and CeO_2 activated LSCM showed the best performance in the fuel cell as well as in electrolysis modes and was also studied in the co-electrolysis mode of H_2O and CO_2. Results indicated that compared to H_2O electrolysis, some of the CO_2 had to be electrochemically reduced at low water partial pressure (0.03 atm) as characteristic diffusion limitation kinetic behavior disappeared during co-electrolysis mode. The production of hydrogen was dominant at lower temperatures, as expected from the lower activation energy of the steam reduction reaction. However, the generation of CO was increased at higher temperatures due to the thermal activation of electrochemical surface processes and increased activity of reverse water gas shift reaction. Pd and CeO_2 activated LSCM also showed high current densities of 1.08 and -1.37 A/cm^2 at 0.5 and 1.6 V in the fuel cell and electrolysis modes, respectively.

8. REFERENCES

[1] D.A.J. Rand, R.M. Dell, Hydrogen Energy: Challenges and Prospects, Royal Society of Chemistry, Cambridge 2007.

[2] S.C. Singhal, K. Kendall, High Temperature Solid oxide Fuel Cells: Fundamentals, Design and Applications, Elsevier, Amsterdam 2003.

[3] M.B. Mogensen, M. Chen, H.L. Frandsen, C. Graves, J.B. Hansen, K.V. Hansen, A. Hauch, T. Jacobsen, S.H. Jensen, T.L. Skafte, X. Sun, Clean Energy 3 (2019) 175–201.

[4] S.Y. Gómez, D. Hotza, Renew. Sustain. Energy Rev. 61 (2016) 155–174.

[5] S.D. Ebbesen, M. Mogensen, J. Power Sources 193 (2009) 349–358.

[6] N.H. Perry, T. Ishihara, Materials 9 (2016) 858–881.

[7] M. Keane, Materials Interactions and Degradation Processes in Solid Oxide Electrolysis Cells, Dr. Diss. (2014). https://opencommons.uconn.edu/ dissertations/ 339 last downloaded 15.12.2019.

[8] Y. Tao, S.D. Ebbesen, M.B. Mogensen, J. Electrochem. Soc. 161 (2014) F337–F343.

[9] S. Tao, J.T.S. Irvine, Nat. Mater. 2 (2003) 320–323.

[10] K.B. Yoo, G.M. Choi, Solid State Ion. 192 (2011) 515–518.

[11] Tao, J.T.S. Irvine, Chem. Mater. 21 (2004) 4116–4121.

[12] K. Tamm, R. Küngas, R.J. Gorte, E. Lust, Electrochimica Acta 106 (2013) 398–405.

[13] B. Ge, J.T. Ma, D. Ai, C. Deng, X. Lin, J. Xu, Electrochimica Acta 151 (2015) 437–446.

[14] Z. Wang, Y. Tian, Y. Li, J. Power Sources 196 (2011) 6104–6109.

[15] S.P. Jiang, Mater. Sci. Eng. A 418 (2006) 199–210.

[16] B.D. Madsen, W. Kobsiriphat, Y. Wang, L.D. Marks, S. Barnett, ECS Trans. 7 (2007) 1339–1348.

[17] D. Neagu, G. Tsekouras, D.N. Miller, H. Ménard, J.T.S. Irvine, Nat. Chem. 5 (2013) 916–923.

[18] H. Uchida, M. Watanabe, High-Performance Electrodes for Medium-Temperature Solid Oxide Fuel Cells, Springer, New York 2008.

[19] J. Larminie, A. Dicks, Fuel cell systems explained, 2nd ed., John Wiley & Sons, Chichester 2003.

[20] N.Q. Minh, T. Takahashi, Science and Technology of Ceramic Fuel Cells, Elsevier, Amsterdam 1995.

[21] S. McIntosh, R.J. Gorte, Chem. Rev. 104 (2004) 4845–4866.

[22] J.T.S. Irvine, P. Connor, Solid Oxide Fuels Cells: Facts and Figures, Springer, London 2013.

[23] N. Mahato, A. Banerjee, A. Gupta, S. Omar, K. Balani, Prog. Mater. Sci. 72 (2015) 141–337.

[24] Y. Arachi, T. Asai, O. Yamamoto, Y. Takeda, N. Imanishi, K. Kawate, C. Tamakoshi, J. Electrochem. Soc. 148 (2001) A520–A523.

[25] T. Ishii, Solid State Ion. 78 (1995) 333–338.

[26] O. Yamamoto, Y. Arati, Y. Takeda, N. Imanishi, Y. Mizutani, M. Kawai, Y. Nakamura, Solid State Ion. 79 (1995) 137–142.

[27] H. Tu, X. Liu, Q. Yu, J. Power Sources. 196 (2011) 3109–3113.

[28] Z. Wang, M. Cheng, Y. Dong, M. Zhang, H. Zhang, J. Power Sources. 156 (2006) 306–310.

[29] S.D. Ebbesen, C. Graves, M. Mogensen, Int. J. Green Energy 6 (2009) 646–660.

[30] N.Q. Minh, M.B. Mogensen, Electrochem. Soc. Interface 22 (2013) 55–62.

[31] X. Sun, M. Chen, Y.-L. Liu, P. Hjalmarsson, S.D. Ebbesen, S.H. Jensen, M.B. Mogensen, P.V. Hendriksen, J. Electrochem. Soc. 160 (2013) F1074–F1080.

[32] S. Zha, Z. Cheng, M. Liu, J. Electrochem. Soc. 154 (2007) B201–B206.

[33] C.H. Bartholomew, Appl. Catal. Gen. 212 (2001) 17–60.

[34] T. Klemensø, C. Chung, P.H. Larsen, M. Mogensen, J. Electrochem. Soc. 152 (2005) A2186–A2192.

[35] A. Faes, A. Hessler-Wyser, A. Zryd, J. Van Herle, Membranes 2 (2012) 585–664.

[36] A. Hauch, S.D. Ebbesen, S.H. Jensen, M. Mogensen, J. Electrochem. Soc. 155 (2008) B1184–B1193.

[37] M.S. Sohal, J.E. O'Brien, C.M. Stoots, V.I. Sharma, B. Yildiz, A. Virkar, J. Fuel Cell Sci. Technol. 9 (2012) 377–387.

[38] M.S. Sohal, J.E. O'Brien, C.M. Stoots, J.J. Hartvigsen, D. Larsen, S. Elangovan, J.S. Herring, J.D. Carter, V.I. Sharma, B. Yildiz, Idaho National Laboratory (2009).

[39] A. Atkinson, S. Barnett, R.J. Gorte, J.T.S. Irvine, A.J. McEvoy, M. Mogensen, S.C. Singhal, J. Vohs, Nat. Mater. 3 (2004) 17–27.

[40] T. Ishihara, Perovskite Oxide for Solid Oxide Fuel Cells, Springer, New York 2009.

[41] T.D. McColm, J.T.S. Irvine, Ionics 7 (2001) 116–121.

[42] C. Jin, C. Yang, F. Zhao, D. Cui, F. Chen, Int. J. Hydrog. Energy 36 (2011) 3340–3346.

[43] Y.-H. Huang, R.I. Dass, Z.-L. Xing, J.B. Goodenough, Science 312 (2006) 254–257.

[44] S. Tao, J.T.S. Irvine, Chem. Mater. 18 (2006) 5453–5460.

[45] S.W. Tao, J.T.S. Irvine, J.A. Kilner, Adv. Mater. 17 (2005) 1734–1737.

[46] S. Zha, P. Tsang, Z. Cheng, M. Liu, J. Solid State Chem. 178 (2005) 1844–1850.

[47] S. Tao, J.T.S. Irvine, J. Electrochem. Soc. 151 (2004) A252–A259.

[48] K. Knížek, J. Hejtmánek, Z. Jirák, C. Martin, M. Hervieu, B. Raveau, G. André, F. Bourée, Chem. Mater. 16 (2004) 1104–1110.

[49] R. Xing, Y. Wang, Y. Zhu, S. Liu, C. Jin, J. Power Sources 274 (2015) 260–264.

[50] C. Ruan, K. Xie, Catal. Sci. Technol. 5 (2015) 1929–1940.

[51] X. Zhang, L. Ye, J. Hu, J. Li, W. Jiang, C.-J. Tseng, K. Xie, Electrochimica Acta. 212 (2016) 32–40.

[52] X. Yue, J.T.S. Irvine, J. Mater. Chem. A 5 (2017) 7081–7090.

[53] X. Yue, J.T.S. Irvine, J. Electrochem. Soc. 159 (2012) F442–F448.

[54] S.P. Jiang, L. Zhang, C.S. Cheng, L. Zhang, ECS Trans. 7 (2007) 1081–1088.

[55] Y. Zheng, R. Ran, Z. Shao, Rare Met. 28 (2009) 361–366.

[56] J.-S. Kim, V.V. Nair, J.M. Vohs, R.J. Gorte, Scr. Mater. 65 (2011) 90–95.

[57] Y. Song, Q. Zhong, W. Tan, Int. J. Hydrog. Energy. 39 (2014) 13694–13700.

[58] X. Zhang, Y. Song, F. Guan, Y. Zhou, H. Lv, G. Wang, X. Bao, J. Catal. 359 (2018) 8–16.

[59] T. Jardiel, M.T. Caldes, F. Moser, J. Hamon, G. Gauthier, O. Joubert, Solid State Ion. 181 (2010) 894–901.

[60] H. Falcón, J.A. Barbero, G. Araujo, M.T. Casais, M.J. Martínez-Lope, J.A. Alonso, J.L.G. Fierro, Appl. Catal. B Environ. 53 (2004) 37–45.

[61] S. Vasala, M. Lehtimäki, Y.H. Huang, H. Yamauchi, J.B. Goodenough, M. Karppinen, J. Solid State Chem. 183 (2010) 1007–1012.

[62] K.-I. Kobayashi, T. Kimura, H. Sawada, K. Terakura, Y. Tokura, Nature 395 (1998) 677–680.

[63] M. Karppinen, H. Yamauchi, Frontiers in Magnetic Materials, Springer, Berlin, Heidelberg 2005.

[64] Q. Liu, X. Dong, G. Xiao, F. Zhao, F. Chen, Adv. Mater. 22 (2010) 5478–5482.

[65] Q. Liu, C. Yang, X. Dong, F. Chen, Int. J. Hydrog. Energy 35 (2010) 10039–10044.

[66] B. He, L. Zhao, S. Song, T. Liu, F. Chen, C. Xia, J. Electrochem. Soc. 159 (2012) B619–B626.

[67] Y. Wang, T. Liu, S. Fang, F. Chen, J. Power Sources 305 (2016) 240–248.

[68] B. Niu, F. Jin, X. Yang, T. Feng, T. He, Int. J. Hydrog. Energy 43 (2018) 3280–3290.

[69] B. He, Z. Wang, L. Zhao, X. Pan, X. Wu, C. Xia, J. Power Sources. 241 (2013) 627–633.

[70] M. Gou, R. Ren, W. Sun, C. Xu, X. Meng, Z. Wang, J. Qiao, K. Sun, Ceram. Int. 45 (2019) 15696–15704.

[71] N. Dai, J. Feng, Z. Wang, T. Jiang, W. Sun, J. Qiao, K. Sun, J. Mater. Chem. A. 1 (2013) 14147–14153.

[72] J. Feng, G. Yang, N. Dai, Z. Wang, W. Sun, D. Rooney, J. Qiao, K. Sun, J. Mater. Chem. A 2 (2014) 17628–17634.

[73] W. Sun, P. Li, C. Xu, L. Dong, J. Qiao, Z. Wang, D. Rooney, K. Sun, J. Power Sources 343 (2017) 237–245.

[74] B. He, C. Gong, Z. Wang, L. Jia, L. Zhao, Int. J. Hydrog. Energy 42 (2017) 10308–10316.

[75] S.P. Jiang, Int. J. Hydrog. Energy 37 (2012) 449–470.

[76] J.M. Vohs, R.J. Gorte, Adv. Mater. 21 (2009) 943–956.

[77] D. Ding, X. Li, S. Yuxiu Lai, K. Gerdes, M. Liu, Energy Environ. Sci. 7 (2014) 552–575.

[78] S.-Y. Lee, R. Aris, Catal. Rev. 27 (1985) 207–340.

[79] M. Komiyama, Catal. Rev. 27 (1985) 341–372.

[80] Y. Li, K. Gerdes, X. Liu, J. Electrochem. Soc. 160 (2013) F554–F559.

[81] G. Kim, S. Lee, J.Y. Shin, G. Corre, J.T.S. Irvine, J.M. Vohs, R.J. Gorte, Electrochem. Solid-State Lett. 12 (2009) B48–B52.

[82] S. Lee, G. Kim, J.M. Vohs, R.J. Gorte, J. Electrochem. Soc. 155 (2008) B1179–B1183.

[83] J. Li, U.G. Singh, J.W. Bennett, K. Page, J.C. Weaver, J.-P. Zhang, T. Proffen, A.M. Rappe, S. Scott, R. Seshadri, Chem. Mater. 19 (2007) 1418–1426.

[84] J. Reedijk, K.R. Poeppelmeier, Comprehensive Inorganic Chemistry II, 2nd ed., Elsevier, Netherlands 2005.

[85] D. Neagu, T.-S. Oh, D.N. Miller, H. Ménard, S.M. Bukhari, S.R. Gamble, R.J. Gorte, J.M. Vohs, J.T.S. Irvine, Nat. Commun. 6 (2015) 1–8.

[86] W. Kobsiriphat, B.D. Madsen, Y. Wang, M. Shah, L.D. Marks, S.A. Barnett, J. Electrochem. Soc. 157 (2010) B279–B284.

[87] J.T.S. Irvine, D. Neagu, M.C. Verbraeken, C. Chatzichristodoulou, C. Graves, M.B. Mogensen, Nat. Energy. 1 (2016) 15014–15039.

[88] S.D. Ebbesen, S.H. Jensen, A. Hauch, M.B. Mogensen, Solid Proton Conducting Cells, and Solid Oxide Cells, Chem. Rev. 114 (2014) 10697–10734.

[89] W. Hay Kan, A. Junio Samson, V. Thangadurai, J. Mater. Chem. A 4 (2016) 17913–17932.

[90] S.F. Corbin, J. Lee, X. Qiao, J. Am. Ceram. Soc. 84 (2001) 41–47.

[91] M. Boaro, J.M. Vohs, R.J. Gorte, J. Am. Ceram. Soc. 86 (2003) 395–400.

[92] K. Tamm, I. Kivi, E. Anderson, A. Trikkel, P. Möller, G. Nurk, E. Lust, J. Electrochem. Soc. 159 (2012) F849–F857.

[93] L. Holzer, B. Münch, B. Iwanschitz, M. Cantoni, Th. Hocker, Th. Graule, J. Power Sources 196 (2011) 7076–7089.

[94] P. Möller, R. Kanarbik, I. Kivi, G. Nurk, E. Lust, J. Electrochem. Soc. 160 (2013) F1245–F1253.

[95] A. Mohammed Hussain, J.V.T. Høgh, T. Jacobsen, N. Bonanos, Int. J. Hydrog. Energy 37 (2012) 4309–4318.

[96] S.D. Ebbesen, X. Sun, M.B. Mogensen, Faraday Discuss. 182 (2015) 393–422.

[97] A.J. Bard, L.R. Faulkner, Electrochemical Methods: Fundamentals and Applications 2nd ed., Wiley, New York 2002.

[98] E. Barsoukov, J.R. Macdonald, Impedance Spectroscopy: Theory, Experiment, and Applications, 2nd ed., John Wiley & Sons, New Jersey 2005.

[99] S. Primdahl, M. Mogensen, J. Electrochem. Soc. 144 (1997) 3409–3419.

[100] S.H. Jensen, A. Hauch, P.V. Hendriksen, M. Mogensen, N. Bonanos, T. Jacobsen, J. Electrochem. Soc. 154 (2007) B1325–B1330.

[101] R. Küngas, I. Kivi, K. Lust, G. Nurk, E. Lust, J. Electroanal. Chem. 629 (2009) 94–101.

[102] J. Nielsen, J. Hjelm, Electroch. Acta 115 (2014) 31–45.

[103] R. Barfod, M. Mogensen, T. Klemensø, A. Hagen, Y.-L. Liu, P.V. Hendriksen, J. Electrochem. Soc. 154 (2007) B371–B378.

[104] L. Adijanto, R. Küngas, F. Bidrawn, R.J. Gorte, J.M. Vohs, J. Power Sources 196 (2011) 5797–5802.

[105] S.-E. Yoon, J.-Y. Ahn, B.-K. Kim, J.-S. Park, Int. J. Hydrog. Energy 40 (2015) 13558–13565.

[106] G. Kim, G. Corre, J.T.S. Irvine, J.M. Vohs, R.J. Gorte, Electrochem. Solid-State Lett. 11 (2008) B16–B19.

[107] M. Maide, K. Lillmaa, L.K. Salvan, P. Möller, M. Uibu, E. Lust, G. Nurk, Fuel Cells 18 (2018) 789–799.

[108] K. Lillmaa, M. Maide, R. Kanarbik, G. Nurk, E. Lust, J. Electrochem. Soc. 163 (2016) F3190–F3196.

[109] M. Maide, K. Lillmaa, G. Nurk, E. Lust, ECS Trans. 78 (2017) 3275–3281.

[110] M. Maide, P. Paiste, P. Möller, E. Lust, G. Nurk, J. Electrochem. Soc. 166 (2019) F1148–F1156.

[111] M.J. Jørgensen, M. Mogensen, J. Electrochem. Soc. 148 (2001) A433–A442.

[112] S. Primdahl, M. Mogensen, J. Electrochem. Soc. 145 (1998) 2431–2438.

[113] G. Kim, G. Corre, J.T.S. Irvine, J.M. Vohs, R.J. Gorte, Electrochem. Solid-State Lett. 11 (2008) B16–B19.

[114] M. Ni, M.K.H. Leung, D.Y.C. Leung, J. Power Sources 163 (2006) 460–466.

[115] S.D. Ebbesen, M. Mogensen, ECS Trans. 50 (2013) 167–182.

[116] S.M. Plint, P.A. Connor, S. Tao, J.T.S. Irvine, Solid State Ion. 177 (2006) 2005–2008.

[117] S. Tao, J.T.S. Irvine, J. Electrochem. Soc. 151 (2004) A252–A259.

[118] H. Ding, A. V. Virkar, M. Liu, F. Liu, Phys. Chem. Chem. Phys. 15 (2013) 489–496.

[119] O. Kwon, S. Sengodan, K. Kim, G. Kim, H.Y. Jeong, J. Shin, Y.-W. Ju, J.W. Han, G. Kim, Nat. Commun. 8 (2017) 1–7.

[120] M.D. Gross, J.M. Vohs, R.J. Gorte, Electrochem. Solid-State Lett. 10 (2007) B65–B69.
[121] S.-W. Kim, H. Kim, K.J. Yoon, J.-H. Lee, B.-K. Kim, W. Choi, J.-H. Lee, J. Hong, J. Power Sources 280 (2015) 630–639.
[122] P. Kim-Lohsoontorn, J. Bae, J. Power Sources 196 (2011) 7161–7168.
[123] C. Stoots, J. O'Brien, J. Hartvigsen, Int. J. Hydrog. Energy 34 (2009) 4208–4215.
[124] C. Graves, S.D. Ebbesen, M. Mogensen, Solid State Ion. 192 (2011) 398–403.
[125] G. Cinti, G. Discepoli, G. Bidini, A. Lanzini, M. Santarelli, Int. J. Energy Res. 40 (2016) 207–215.

9. SUMMARY IN ESTONIAN

Segajuhtelektroodide mikrostruktuuri ja keemilise koostise mõju pööratava funktsionaalsusega tahkeoksiidsete kütuseelementide elektrokeemilisele käitumisele

Antud doktoritöö raames valmistati ja karakteriseeriti pööratava funktsionaalsusega tahkeoksiidseid kütuseelemente, kasutades $(La_{1-x}Sr_x)_yCr_{0.5-z}Mn_{0.5-w}Ni_{z+w}O_{3-\delta}$, CeO_2 ning Pd nanoosakestega infiltreeritud $La_{0.8}Sr_{0.2}Cr_{0.5}Mn_{0.5}O_{3-\delta}$ ja $Sr_xFe_{1-y}Mo_yO_{6-\delta}$ segajuhtmaterjalidel põhinevaid keraamilisi elektroodimaterjale.

Töö esimeses osas analüüsiti uuritavate ühikrakkude komplekstakistuse muutumist nii süsteemi temperatuuri, gaasisegude koostise kui ka potentsiaali varieerimise tagajärjel. Tekkivaid muutusi visualiseeriti impedantsspektri erinevusanalüüsi meetodit (ADIS) kasutades. Vesiniku osarõhu, pH_2, varieerimisel leidsid suurimad muutused aset 0.5 Hz ümbruses, kus on summaarset elektrokeemilist reaktsiooni limiteerivaks tahkis-gaas piirpinnal toimuvad sorptsiooniprotsessid. Ei peetud tõenäoliseks, et limiteerivaks protsessiks on gaasikontsentratsiooni muutusest tingitud impedants. $(La_{1-x}Sr_x)_yCr_{0.5-z}Mn_{0.5-w}Ni_{z+w}O_{3-\delta}$ kompleksoksiidi B-saidi Ni sisalduse suurenedamine Mn arvelt parandas materjali elektronjuhtivust, ning tõstis seeläbi elektroodi vesiniku adsorptsiooni ja dissotsiatsiooniga seotud katalüütilist aktiivsust. Hapniku osarõhu, pO_2, varieerimine hapnikuelektroodil põhjustas väikseid muutusi $(La_{1-x}Sr_x)_yCr_{0.5-z}Mn_{0.5-w}Ni_{z+w}O_{3-\delta}|ScCeSZ|La_{0.8}Sr_{0.2}FeO_{3-\delta}$ ühikraku komplekstakistuses, aga polnud summaarset protsessi limiteerivaks.

Töö teises osas näidati, et ScCeSZ elektrolüüdi toorpulbri eelpaagutamine suurendas valmistatud elektrolüüdimaatriksi avatud poorsust umbes 10 mahuprotsenti, põhjustades elektrokeemilise aktiivsuse langemist madalamatel segajuhi infiltreerimiskogustel. Seetõttu olid madalamate segajuhi infiltreerimiskoguste korral elektrokeemiliselt aktiivsemad töötlemata elektrolüüdi toorpulbrist valmistatud poorsetel struktuuridel põhinevad elektroodid. Infiltreerimiskoguste suurenemisel olid elektrokeemiliselt aktiivsemad suurema algpoorsusega elektrolüüdimaatriksil põhinevad elektroodid.

Töö kolmandas osas uuriti segajuhtelektroodide keemilise koostise muutmise mõju pööratava funktsionaalsusega tahkeoksiidkütuseelemendi ühikrakkude elektrokeemilisele käitumisele. Leiti, et segajuhtmaterjalide keemilise koostise modifitseerimise tulemusena väheneb $La_{0.75}Sr_{0.25}Cr_{0.50}Mn_{0.30}Ni_{0.20}O_{3-\delta}$-i kasutava ühikraku polarisatsiooniline takistus kolm korda, kui see asendati $La_{0.75}Sr_{0.25}Cr_{0.30}Mn_{0.50}Ni_{0.20}O_{3-\delta}$ segajuhtmaterjaliga. Sellist elektrokeemilise käitumise muutust seletati oksiidioonvakantside hulgaga kristallvõres, mis sõltus ennekõike Mn kontsentratsioonist perovskiitse materjali B-saidis ja selle võimest oksüdatsiooniastet muuta. Võrreldes $La_{0.75}Sr_{0.25}Cr_{0.50}Mn_{0.30}Ni_{0.20}O_{3-\delta}$ anoodimaterjaliga näitas sarnase Cr sisaldusega, aga madalama Ni sisaldusega ja mõõduka A-saidi defitsiidiga $(La_{0.8}Sr_{0.2})_{0.95}Cr_{0.49}Mn_{0.49}Ni_{0.02}O_{3-\delta}$ anoodimaterjal üle kahe korra madalamat polarisatsioonilist takistust. Saadud tulemused kinnitavad, et segajuhtelektroodide elektrokeemiline aktiivsus on väga kompleksne omadus ja sõltub nii ioonjuhtivuse, elektronjuhtivuse kui ka pinna katalüütiliste omaduste hapniku osarõhu sõltuvusest.

Uuritud materjalidest näitas parimat elektrokeemilist aktiivsust nii kütuseelemendi kui ka elektrolüüsirežiimis Pd ja CeO_2 nanoosakestega aktiveeritud $La_{0.80}Sr_{0.20}Cr_{0.50}Mn_{0.50}O_{3-\delta}$ keraamiline anoodimaterjal, mida karakteriseeriti H_2O ja CO_2 kaaselektrolüüsi režiimis. Leidis kinnitust, et lisaks vesigaasi reaktsiooni termodünaamilisele tasakaalule, leiab CO süntees aset ka elektrokeemilise reaktsiooni tagajärjel. Samuti leiti, et madalamal temperatuuril oli H_2O redutseerumise väiksema aktivatsioonienergia tõttu soodustatud H_2 tekkimine. Kõrgematel temperatuuridel suurenes aga CO osakaal nii kiirema CO_2 redutseerumise kui ka vesigaasi reaktsiooni termodünaamilise tasakaalu nihkumise tõttu CO tekke suunas. Uuritud elektrokeemiline rakk näitas väga head elektrokeemilist aktiivsust nii kütuseelemendi režiimis 0.5 V (1.08 A/cm^2) juures kui ka elektrolüüsi režiimis 1.6 V juures (-1.37 A/cm^2).

10. ACKNOWLEDGMENTS

Firstly, I would like to express the deepest gratitude to my supervisors, Gunnar Nurk and Prof. Enn Lust. Gunnar, you have always pushed me to see the wider picture, for which I am most grateful. Thank you for your multitude of ideas – the conversations have been anything but boring. Enn, thank you for showing where enthusiasm and hard work can take a person. Also, thank you for your everlasting patience, your ever wider scientific worldview as well as the knowledge on the energy industry all around the world. You have provided me with everything a student could ever wish for.

I would also like to thank Dr. Priit Möller for TOF-SIMS measurements; Dr. Päärn Paiste for LA-ICP-MS measurements; Mr. Jaan Aruväli for XRD measurements; Prof. Kalle Kirsimäe for the help with the SEM measurements; Dr. Mai Uibu for Mercury intrusion porosimetry measurements.

I could not thank enough Rait Kanarbik for technical support and making me read the manuals and Dr. Rasmus Palm for interesting discussions. Most importantly, I would like to thank Ove Korjus, Alar Heinsaar and Ronald Väli for bearing with me – you are the best. I want to thank all the colleagues from the chair of physical chemistry for interesting discussions, great ideas and, in general, an academically enjoyable time.

I would not be where and who I am without my loving and supporting family. Dearest Laura and Herbert, I love you more than words could ever express, you are my everything.

This research was supported by the EU through the European Regional Development Fund (Centers of Excellence, TK141 2014-2020.4.01.15-0011 and TK117 3.2.0101-0030; project SLOKT12181T 3.2.1101.12-0014; project SLOKT10209T; Higher education specialization stipends in smart specialization growth areas 2014-2020.4.02.16-0026 and Graduate School of Functional materials and technologies in University of Tartu). This work was partially supported by Estonian Research Council Institutional Grant IUT20-13, ETF9352, personal research grants PUT1581 and PRG551.

PUBLICATIONS

CURRICULUM VITAE

Name: Martin Maide
Date of birth: February 3, 1991
Citizenship: Estonian
Contact: Institute of Chemistry, University of Tartu
Ravila 14a, 50411, Tartu, Estonia
E-mail: martin.maide@ut.ee

Education:

2015–…	University of Tartu, Institute of Chemistry, PhD student
2013–2015	University of Tartu – Master's degree in chemistry
2010–2013	University of Tartu – Bachelor's degree in chemistry

Professional Employment:

2012–…	University of Tartu, Institute of Chemistry, Chemist

List of publications:

1. M. Vestli, M. Maide, G. Nurk, E. Lust, Characterization of Doped Ceria Films as SOFC Electrolyte Prepared by Using Ultrasonic Spray Pyrolysis Method, ECS Transactions 57 (1) (2013) 1159−1165.
2. M. Maide, O. Korjus, M. Vestli, E. Lust, G. Nurk, Protective yttrium doped barium zirconate layer on yttrium doped barium cerate proton conductive membrane, ECS Transactions 57 (1) (2013) 1151−1157.
3. M. Maide, O. Korjus, M. Vestli, T. Romann, G. Nurk, Comparative Study of $BaY_{0.1}Ce_{0.9}O_{3-\delta}$ Membrane with $BaY_{0.1}Zr_{0.9}O_{3-\delta}$ Protective Layers Synthesized with Spray Pyrolysis and Magnetron Sputtering Methods, ECS Transactions 68 (1) (2015) 473−480.
4. K. Lillmaa, M. Maide, R. Kanarbik, G. Nurk, E. Lust, Electrochemical Characteristics and Gas Composition Generated by $La_{0.8}Sr_{0.2}Cr_{0.5}Mn_{0.5}O_{3-\delta}$ Cathode at Electrolysis and Co-Electrolysis Modes, Journal of the Electrochemical Society 163 (11) (2016) F3190−F3196.
5. M. Maide, O. Korjus, M. Vestli, T. Romann, J. Aruväli, K. Kirsimäe, G. Nurk, Comparative Study of $BaY_{0.1}Zr_{0.9}O_{3-\delta}$ Protective Layers Deposited to $BaY_{0.1}Ce_{0.9}O_{3-\delta}$ Membrane Using Ultrasonic Spray Pyrolysis and Magnetron Sputtering Methods, Journal of the Electrochemical Society 163 (5) (2016) F443−F447.
6. E. Lust, K. Lillmaa, G. Nurk, R. Kanarbik, P. Möller, I. Kivi, M. Vestli, M. Maide, O. Korjus, L. K. Salvan, F. Kukk, Development of Ceramic Materials and Application of Novel Physical Analysis Methods to Enhance Solid Oxide Fuel Cells and Solid Oxide Electrolysis Cells, ECS Transactions 78 (1) (2017) 3229−3236.
7. M. Maide, K. Lillmaa, G. Nurk, E. Lust, Dependence of Syn-Gas Composition on Microstructure of $La_{0.8}Sr_{0.2}Cr_{0.5}Mn_{0.5}O_{3-\delta}$ Based Cathode for

CO_2 and H_2O Co-Electrolysis, ECS Transactions 78 (1) (2017) 3275−3281.

8. M. Maide, K. Lillmaa, L. K. Salvan, P. Möller, E. Lust, G. Nurk, Influence of Electrolyte Scaffold Microstructure and Loading of MIEC Material on the Electrochemical Performance of RSOC Fuel Electrode, Book of Abstracts: 7th Baltic Electrochemistry Conference (2018) 89.
9. M. Maide, K. Lillmaa, L. K. Salvan, P. Möller, M. Uibu, E. Lust, G. Nurk, Influence of Electrolyte Scaffold Microstructure and Loading of MIEC Material on the Electrochemical Performance of RSOC Fuel Electrode, Fuel Cells, 18 (6) (2018) 789−799.
10. O. Korjus, G. Nurk, J. Aruväli, I. Kivi, M. Maide, E. Lust, Electrochemical- and Crystallographic Operando Characterization of $La_{0.75}Sr_{0.25}Cr_{0.5}Mn_{0.3}Ni_{0.2}O_{3-\delta}$ Anode Infiltrated into $Sc_{0.2}Ce_{0.01}Zr_{0.79}O_{2-\delta}$ Electrolyte Scaffold, ECS Transactions 91 (1) (2019) 1683−1692.
11. M. Maide, P. Möller, G. Nurk, E. Lust, Influence of A-Site Deficiency, Porous Electrolyte Scaffold and Loading of MIEC Material on the Performance of $La_{0.8}Sr_{0.2}Cr_{0.5}Mn_{0.5}O_{3-\delta}$ Based R-SOC Fuel Electrode, ECS Transactions 91 (1) (2019) 2369−2377.
12. M. Maide, P. Paiste, P. Möller, E. Lust, G. Nurk, Influence of A- and B-Site Modifications of $(La_{1-x}Sr_x)_yCr_{0.5-z}Mn_{0.5-w}Ni_{z+w}O_{3-\delta}$ on Electrochemical Impedance Characteristics of Reversible Solid Oxide Cell, Journal of the Electrochemical Society 166 (15) (2019) F1148−F1156.

ELULOOKIRJELDUS

Nimi: Martin Maide
Sünniaeg: 3. veebruar 1991
Kodakondsus: Eesti
Aadress: Keemia instituut, Tartu Ülikool
Ravila 14a, 50411, Tartu, Eesti
E-post: martin.maide@ut.ee

Haridustee:

2015–…	Tartu Ülikool, Keemia instituut, doktorant
2013–2015	Tartu Ülikool – Magistrikraad keemias
2010–2013	Tartu Ülikool – Bakalaureusekraad keemias

Teenistuskäik:

2012–…	Tartu Ülikool, Keemia instituut, keemik

Teaduspublikatsioonid:

1. M. Vestli, M. Maide, G. Nurk, E. Lust, Characterization of Doped Ceria Films as SOFC Electrolyte Prepared by Using Ultrasonic Spray Pyrolysis Method, ECS Transactions 57 (1) (2013) 1159−1165.
2. M. Maide, O. Korjus, M. Vestli, E. Lust, G. Nurk, Protective yttrium doped barium zirconate layer on yttrium doped barium cerate proton conductive membrane, ECS Transactions 57 (1) (2013) 1151−1157.
3. M. Maide, O. Korjus, M. Vestli, T. Romann, G. Nurk, Comparative Study of $\mathrm{BaY_{0.1}Ce_{0.9}O_{3-\delta}}$ Membrane with $\mathrm{BaY_{0.1}Zr_{0.9}O_{3-\delta}}$ Protective Layers Synthesized with Spray Pyrolysis and Magnetron Sputtering Methods, ECS Transactions 68 (1) (2015) 473−480.
4. K. Lillmaa, M. Maide, R. Kanarbik, G. Nurk, E. Lust, Electrochemical Characteristics and Gas Composition Generated by $\mathrm{La_{0.8}Sr_{0.2}Cr_{0.5}Mn_{0.5}O_{3-\delta}}$ Cathode at Electrolysis and Co-Electrolysis Modes, Journal of the Electrochemical Society 163 (11) (2016) F3190−F3196.
5. M. Maide, O. Korjus, M. Vestli, T. Romann, J. Aruväli, K. Kirsimäe, G. Nurk, Comparative Study of $\mathrm{BaY_{0.1}Zr_{0.9}O_{3-\delta}}$ Protective Layers Deposited to $\mathrm{BaY_{0.1}Ce_{0.9}O_{3-\delta}}$ Membrane Using Ultrasonic Spray Pyrolysis and Magnetron Sputtering Methods, Journal of the Electrochemical Society 163 (5) (2016) F443−F447.
6. E. Lust, K. Lillmaa, G. Nurk, R. Kanarbik, P. Möller, I. Kivi, M. Vestli, M. Maide, O. Korjus, L. K. Salvan, F. Kukk, Development of Ceramic Materials and Application of Novel Physical Analysis Methods to Enhance Solid Oxide Fuel Cells and Solid Oxide Electrolysis Cells, ECS Transactions 78 (1) (2017) 3229−3236.
7. M. Maide, K. Lillmaa, G. Nurk, E. Lust, Dependence of Syn-Gas Composition on Microstructure of $\mathrm{La_{0.8}Sr_{0.2}Cr_{0.5}Mn_{0.5}O_{3-\delta}}$ Based Cathode for

CO_2 and H_2O Co-Electrolysis, ECS Transactions 78 (1) (2017) 3275−3281.

8. M. Maide, K. Lillmaa, L. K. Salvan, P. Möller, E. Lust, G. Nurk, Influence of Electrolyte Scaffold Microstructure and Loading of MIEC Material on the Electrochemical Performance of RSOC Fuel Electrode, Book of Abstracts: 7th Baltic Electrochemistry Conference (2018) 89.
9. M. Maide, K. Lillmaa, L. K. Salvan, P. Möller, M. Uibu, E. Lust, G. Nurk, Influence of Electrolyte Scaffold Microstructure and Loading of MIEC Material on the Electrochemical Performance of RSOC Fuel Electrode, Fuel Cells, 18 (6) (2018) 789−799.
10. O. Korjus, G. Nurk, J. Aruväli, I. Kivi, M. Maide, E. Lust, Electrochemical- and Crystallographic Operando Characterization of $La_{0.75}Sr_{0.25}Cr_{0.5}Mn_{0.3}Ni_{0.2}O_{3-\delta}$ Anode Infiltrated into $Sc_{0.2}Ce_{0.01}Zr_{0.79}O_{2-\delta}$ Electrolyte Scaffold, ECS Transactions 91 (1) (2019) 1683−1692.
11. M. Maide, P. Möller, G. Nurk, E. Lust, Influence of A-Site Deficiency, Porous Electrolyte Scaffold and Loading of MIEC Material on the Performance of $La_{0.8}Sr_{0.2}Cr_{0.5}Mn_{0.5}O_{3-\delta}$ Based R-SOC Fuel Electrode, ECS Transactions 91 (1) (2019) 2369−2377.
12. M. Maide, P. Paiste, P. Möller, E. Lust, G. Nurk, Influence of A- and B-Site Modifications of $(La_{1-x}Sr_x)_yCr_{0.5-z}Mn_{0.5-w}Ni_{z+w}O_{3-\delta}$ on Electrochemical Impedance Characteristics of Reversible Solid Oxide Cell, Journal of the Electrochemical Society 166 (15) (2019) F1148−F1156.

DISSERTATIONES CHIMICAE UNIVERSITATIS TARTUENSIS

1. **Toomas Tamm.** Quantum-chemical simulation of solvent effects. Tartu, 1993, 110 p.
2. **Peeter Burk.** Theoretical study of gas-phase acid-base equilibria. Tartu, 1994, 96 p.
3. **Victor Lobanov.** Quantitative structure-property relationships in large descriptor spaces. Tartu, 1995, 135 p.
4. **Vahur Mäemets.** The ^{17}O and ^{1}H nuclear magnetic resonance study of H_2O in individual solvents and its charged clusters in aqueous solutions of electrolytes. Tartu, 1997, 140 p.
5. **Andrus Metsala.** Microcanonical rate constant in nonequilibrium distribution of vibrational energy and in restricted intramolecular vibrational energy redistribution on the basis of slater's theory of unimolecular reactions. Tartu, 1997, 150 p.
6. **Uko Maran.** Quantum-mechanical study of potential energy surfaces in different environments. Tartu, 1997, 137 p.
7. **Alar Jänes.** Adsorption of organic compounds on antimony, bismuth and cadmium electrodes. Tartu, 1998, 219 p.
8. **Kaido Tammeveski.** Oxygen electroreduction on thin platinum films and the electrochemical detection of superoxide anion. Tartu, 1998, 139 p.
9. **Ivo Leito.** Studies of Brønsted acid-base equilibria in water and non-aqueous media. Tartu, 1998, 101 p.
10. **Jaan Leis.** Conformational dynamics and equilibria in amides. Tartu, 1998, 131 p.
11. **Toonika Rinken.** The modelling of amperometric biosensors based on oxidoreductases. Tartu, 2000, 108 p.
12. **Dmitri Panov.** Partially solvated Grignard reagents. Tartu, 2000, 64 p.
13. **Kaja Orupõld.** Treatment and analysis of phenolic wastewater with microorganisms. Tartu, 2000, 123 p.
14. **Jüri Ivask.** Ion Chromatographic determination of major anions and cations in polar ice core. Tartu, 2000, 85 p.
15. **Lauri Vares.** Stereoselective Synthesis of Tetrahydrofuran and Tetrahydropyran Derivatives by Use of Asymmetric Horner-Wadsworth-Emmons and Ring Closure Reactions. Tartu, 2000, 184 p.
16. **Martin Lepiku.** Kinetic aspects of dopamine D_2 receptor interactions with specific ligands. Tartu, 2000, 81 p.
17. **Katrin Sak.** Some aspects of ligand specificity of P2Y receptors. Tartu, 2000, 106 p.
18. **Vello Pällin.** The role of solvation in the formation of iotsitch complexes. Tartu, 2001, 95 p.
19. **Katrin Kollist.** Interactions between polycyclic aromatic compounds and humic substances. Tartu, 2001, 93 p.

20. **Ivar Koppel.** Quantum chemical study of acidity of strong and superstrong Brønsted acids. Tartu, 2001, 104 p.
21. **Viljar Pihl.** The study of the substituent and solvent effects on the acidity of OH and CH acids. Tartu, 2001, 132 p.
22. **Natalia Palm.** Specification of the minimum, sufficient and significant set of descriptors for general description of solvent effects. Tartu, 2001, 134 p.
23. **Sulev Sild.** QSPR/QSAR approaches for complex molecular systems. Tartu, 2001, 134 p.
24. **Ruslan Petrukhin.** Industrial applications of the quantitative structure-property relationships. Tartu, 2001, 162 p.
25. **Boris V. Rogovoy.** Synthesis of (benzotriazolyl)carboximidamides and their application in relations with *N*- and *S*-nucleophyles. Tartu, 2002, 84 p.
26. **Koit Herodes.** Solvent effects on UV-vis absorption spectra of some solvatochromic substances in binary solvent mixtures: the preferential solvation model. Tartu, 2002, 102 p.
27. **Anti Perkson.** Synthesis and characterisation of nanostructured carbon. Tartu, 2002, 152 p.
28. **Ivari Kaljurand.** Self-consistent acidity scales of neutral and cationic Brønsted acids in acetonitrile and tetrahydrofuran. Tartu, 2003, 108 p.
29. **Karmen Lust.** Adsorption of anions on bismuth single crystal electrodes. Tartu, 2003, 128 p.
30. **Mare Piirsalu.** Substituent, temperature and solvent effects on the alkaline hydrolysis of substituted phenyl and alkyl esters of benzoic acid. Tartu, 2003, 156 p.
31. **Meeri Sassian.** Reactions of partially solvated Grignard reagents. Tartu, 2003, 78 p.
32. **Tarmo Tamm.** Quantum chemical modelling of polypyrrole. Tartu, 2003. 100 p.
33. **Erik Teinemaa.** The environmental fate of the particulate matter and organic pollutants from an oil shale power plant. Tartu, 2003. 102 p.
34. **Jaana Tammiku-Taul.** Quantum chemical study of the properties of Grignard reagents. Tartu, 2003. 120 p.
35. **Andre Lomaka.** Biomedical applications of predictive computational chemistry. Tartu, 2003. 132 p.
36. **Kostyantyn Kirichenko.** Benzotriazole – Mediated Carbon–Carbon Bond Formation. Tartu, 2003. 132 p.
37. **Gunnar Nurk.** Adsorption kinetics of some organic compounds on bismuth single crystal electrodes. Tartu, 2003, 170 p.
38. **Mati Arulepp.** Electrochemical characteristics of porous carbon materials and electrical double layer capacitors. Tartu, 2003, 196 p.
39. **Dan Cornel Fara.** QSPR modeling of complexation and distribution of organic compounds. Tartu, 2004, 126 p.
40. **Riina Mahlapuu.** Signalling of galanin and amyloid precursor protein through adenylate cyclase. Tartu, 2004, 124 p.

41. **Mihkel Kerikmäe.** Some luminescent materials for dosimetric applications and physical research. Tartu, 2004, 143 p.
42. **Jaanus Kruusma.** Determination of some important trace metal ions in human blood. Tartu, 2004, 115 p.
43. **Urmas Johanson.** Investigations of the electrochemical properties of polypyrrole modified electrodes. Tartu, 2004, 91 p.
44. **Kaido Sillar.** Computational study of the acid sites in zeolite ZSM-5. Tartu, 2004, 80 p.
45. **Aldo Oras.** Kinetic aspects of dATPαS interaction with P2Y$_1$ receptor. Tartu, 2004, 75 p.
46. **Erik Mölder.** Measurement of the oxygen mass transfer through the air-water interface. Tartu, 2005, 73 p.
47. **Thomas Thomberg.** The kinetics of electroreduction of peroxodisulfate anion on cadmium (0001) single crystal electrode. Tartu, 2005, 95 p.
48. **Olavi Loog.** Aspects of condensations of carbonyl compounds and their imine analogues. Tartu, 2005, 83 p.
49. **Siim Salmar.** Effect of ultrasound on ester hydrolysis in aqueous ethanol. Tartu, 2006, 73 p.
50. **Ain Uustare.** Modulation of signal transduction of heptahelical receptors by other receptors and G proteins. Tartu, 2006, 121 p.
51. **Sergei Yurchenko.** Determination of some carcinogenic contaminants in food. Tartu, 2006, 143 p.
52. **Kaido Tämm.** QSPR modeling of some properties of organic compounds. Tartu, 2006, 67 p.
53. **Olga Tšubrik.** New methods in the synthesis of multisubstituted hydrazines. Tartu. 2006, 183 p.
54. **Lilli Sooväli.** Spectrophotometric measurements and their uncertainty in chemical analysis and dissociation constant measurements. Tartu, 2006, 125 p.
55. **Eve Koort.** Uncertainty estimation of potentiometrically measured ph and pK_a values. Tartu, 2006, 139 p.
56. **Sergei Kopanchuk.** Regulation of ligand binding to melanocortin receptor subtypes. Tartu, 2006, 119 p.
57. **Silvar Kallip.** Surface structure of some bismuth and antimony single crystal electrodes. Tartu, 2006, 107 p.
58. **Kristjan Saal.** Surface silanization and its application in biomolecule coupling. Tartu, 2006, 77 p.
59. **Tanel Tätte.** High viscosity Sn(OBu)$_4$ oligomeric concentrates and their applications in technology. Tartu, 2006, 91 p.
60. **Dimitar Atanasov Dobchev**. Robust QSAR methods for the prediction of properties from molecular structure. Tartu, 2006, 118 p.
61. **Hannes Hagu**. Impact of ultrasound on hydrophobic interactions in solutions. Tartu, 2007, 81 p.
62. **Rutha Jäger.** Electroreduction of peroxodisulfate anion on bismuth electrodes. Tartu, 2007, 142 p.

63. **Kaido Viht.** Immobilizable bisubstrate-analogue inhibitors of basophilic protein kinases: development and application in biosensors. Tartu, 2007, 88 p.
64. **Eva-Ingrid Rõõm.** Acid-base equilibria in nonpolar media. Tartu, 2007, 156 p.
65. **Sven Tamp.** DFT study of the cesium cation containing complexes relevant to the cesium cation binding by the humic acids. Tartu, 2007, 102 p.
66. **Jaak Nerut.** Electroreduction of hexacyanoferrate(III) anion on Cadmium (0001) single crystal electrode. Tartu, 2007, 180 p.
67. **Lauri Jalukse.** Measurement uncertainty estimation in amperometric dissolved oxygen concentration measurement. Tartu, 2007, 112 p.
68. **Aime Lust.** Charge state of dopants and ordered clusters formation in CaF_2:Mn and CaF_2:Eu luminophors. Tartu, 2007, 100 p.
69. **Iiris Kahn**. Quantitative Structure-Activity Relationships of environmentally relevant properties. Tartu, 2007, 98 p.
70. **Mari Reinik.** Nitrates, nitrites, N-nitrosamines and polycyclic aromatic hydrocarbons in food: analytical methods, occurrence and dietary intake. Tartu, 2007, 172 p.
71. **Heili Kasuk.** Thermodynamic parameters and adsorption kinetics of organic compounds forming the compact adsorption layer at Bi single crystal electrodes. Tartu, 2007, 212 p.
72. **Erki Enkvist.** Synthesis of adenosine-peptide conjugates for biological applications. Tartu, 2007, 114 p.
73. **Svetoslav Hristov Slavov**. Biomedical applications of the QSAR approach. Tartu, 2007, 146 p.
74. **Eneli Härk.** Electroreduction of complex cations on electrochemically polished Bi(*hkl*) single crystal electrodes. Tartu, 2008, 158 p.
75. **Priit Möller.** Electrochemical characteristics of some cathodes for medium temperature solid oxide fuel cells, synthesized by solid state reaction technique. Tartu, 2008, 90 p.
76. **Signe Viggor.** Impact of biochemical parameters of genetically different pseudomonads at the degradation of phenolic compounds. Tartu, 2008, 122 p.
77. **Ave Sarapuu.** Electrochemical reduction of oxygen on quinone-modified carbon electrodes and on thin films of platinum and gold. Tartu, 2008, 134 p.
78. **Agnes Kütt.** Studies of acid-base equilibria in non-aqueous media. Tartu, 2008, 198 p.
79. **Rouvim Kadis.** Evaluation of measurement uncertainty in analytical chemistry: related concepts and some points of misinterpretation. Tartu, 2008, 118 p.
80. **Valter Reedo.** Elaboration of IVB group metal oxide structures and their possible applications. Tartu, 2008, 98 p.
81. **Aleksei Kuznetsov.** Allosteric effects in reactions catalyzed by the cAMP-dependent protein kinase catalytic subunit. Tartu, 2009, 133 p.

82. **Aleksei Bredihhin.** Use of mono- and polyanions in the synthesis of multisubstituted hydrazine derivatives. Tartu, 2009, 105 p.
83. **Anu Ploom.** Quantitative structure-reactivity analysis in organosilicon chemistry. Tartu, 2009, 99 p.
84. **Argo Vonk.** Determination of adenosine A_{2A}- and dopamine D_1 receptor-specific modulation of adenylate cyclase activity in rat striatum. Tartu, 2009, 129 p.
85. **Indrek Kivi.** Synthesis and electrochemical characterization of porous cathode materials for intermediate temperature solid oxide fuel cells. Tartu, 2009, 177 p.
86. **Jaanus Eskusson.** Synthesis and characterisation of diamond-like carbon thin films prepared by pulsed laser deposition method. Tartu, 2009, 117 p.
87. **Marko Lätt.** Carbide derived microporous carbon and electrical double layer capacitors. Tartu, 2009, 107 p.
88. **Vladimir Stepanov.** Slow conformational changes in dopamine transporter interaction with its ligands. Tartu, 2009, 103 p.
89. **Aleksander Trummal.** Computational Study of Structural and Solvent Effects on Acidities of Some Brønsted Acids. Tartu, 2009, 103 p.
90. **Eerold Vellemäe.** Applications of mischmetal in organic synthesis. Tartu, 2009, 93 p.
91. **Sven Parkel.** Ligand binding to 5-HT_{1A} receptors and its regulation by Mg^{2+} and Mn^{2+}. Tartu, 2010, 99 p.
92. **Signe Vahur.** Expanding the possibilities of ATR-FT-IR spectroscopy in determination of inorganic pigments. Tartu, 2010, 184 p.
93. **Tavo Romann**. Preparation and surface modification of bismuth thin film, porous, and microelectrodes. Tartu, 2010, 155 p.
94. **Nadežda Aleksejeva.** Electrocatalytic reduction of oxygen on carbon nanotube-based nanocomposite materials. Tartu, 2010, 147 p.
95. **Marko Kullapere.** Electrochemical properties of glassy carbon, nickel and gold electrodes modified with aryl groups. Tartu, 2010, 233 p.
96. **Liis Siinor.** Adsorption kinetics of ions at Bi single crystal planes from aqueous electrolyte solutions and room-temperature ionic liquids. Tartu, 2010, 101 p.
97. **Angela Vaasa.** Development of fluorescence-based kinetic and binding assays for characterization of protein kinases and their inhibitors. Tartu 2010, 101 p.
98. **Indrek Tulp.** Multivariate analysis of chemical and biological properties. Tartu 2010, 105 p.
99. **Aare Selberg.** Evaluation of environmental quality in Northern Estonia by the analysis of leachate. Tartu 2010, 117 p.
100. **Darja Lavõgina.** Development of protein kinase inhibitors based on adenosine analogue-oligoarginine conjugates. Tartu 2010, 248 p.
101. **Laura Herm.** Biochemistry of dopamine D_2 receptors and its association with motivated behaviour. Tartu 2010, 156 p.

102. **Terje Raudsepp.** Influence of dopant anions on the electrochemical properties of polypyrrole films. Tartu 2010, 112 p.
103. **Margus Marandi.** Electroformation of Polypyrrole Films: *In-situ* AFM and STM Study. Tartu 2011, 116 p.
104. **Kairi Kivirand.** Diamine oxidase-based biosensors: construction and working principles. Tartu, 2011, 140 p.
105. **Anneli Kruve.** Matrix effects in liquid-chromatography electrospray mass-spectrometry. Tartu, 2011, 156 p.
106. **Gary Urb.** Assessment of environmental impact of oil shale fly ash from PF and CFB combustion. Tartu, 2011, 108 p.
107. **Nikita Oskolkov.** A novel strategy for peptide-mediated cellular delivery and induction of endosomal escape. Tartu, 2011, 106 p.
108. **Dana Martin.** The QSPR/QSAR approach for the prediction of properties of fullerene derivatives. Tartu, 2011, 98 p.
109. **Säde Viirlaid.** Novel glutathione analogues and their antioxidant activity. Tartu, 2011, 106 p.
110. **Ülis Sõukand.** Simultaneous adsorption of Cd^{2+}, Ni^{2+}, and Pb^{2+} on peat. Tartu, 2011, 124 p.
111. **Lauri Lipping.** The acidity of strong and superstrong Brønsted acids, an outreach for the “limits of growth”: a quantum chemical study. Tartu, 2011, 124 p.
112. **Heisi Kurig.** Electrical double-layer capacitors based on ionic liquids as electrolytes. Tartu, 2011, 146 p.
113. **Marje Kasari.** Bisubstrate luminescent probes, optical sensors and affinity adsorbents for measurement of active protein kinases in biological samples. Tartu, 2012, 126 p.
114. **Kalev Takkis.** Virtual screening of chemical databases for bioactive molecules. Tartu, 2012, 122 p.
115. **Ksenija Kisseljova**. Synthesis of aza-β^3-amino acid containing peptides and kinetic study of their phosphorylation by protein kinase A. Tartu, 2012, 104 p.
116. **Riin Rebane.** Advanced method development strategy for derivatization LC/ESI/MS. Tartu, 2012, 184 p.
117. **Vladislav Ivaništšev.** Double layer structure and adsorption kinetics of ions at metal electrodes in room temperature ionic liquids. Tartu, 2012, 128 p.
118. **Irja Helm.** High accuracy gravimetric Winkler method for determination of dissolved oxygen. Tartu, 2012, 139 p.
119. **Karin Kipper.** Fluoroalcohols as Components of LC-ESI-MS Eluents: Usage and Applications. Tartu, 2012, 164 p.
120. **Arno Ratas.** Energy storage and transfer in dosimetric luminescent materials. Tartu, 2012, 163 p.
121. **Reet Reinart-Okugbeni**. Assay systems for characterisation of subtype-selective binding and functional activity of ligands on dopamine receptors. Tartu, 2012, 159 p.

122. **Lauri Sikk.** Computational study of the Sonogashira cross-coupling reaction. Tartu, 2012, 81 p.
123. **Karita Raudkivi.** Neurochemical studies on inter-individual differences in affect-related behaviour of the laboratory rat. Tartu, 2012, 161 p.
124. **Indrek Saar.** Design of GalR2 subtype specific ligands: their role in depression-like behavior and feeding regulation. Tartu, 2013, 126 p.
125. **Ann Laheäär.** Electrochemical characterization of alkali metal salt based non-aqueous electrolytes for supercapacitors. Tartu, 2013, 127 p.
126. **Kerli Tõnurist.** Influence of electrospun separator materials properties on electrochemical performance of electrical double-layer capacitors. Tartu, 2013, 147 p.
127. **Kaija Põhako-Esko.** Novel organic and inorganic ionogels: preparation and characterization. Tartu, 2013, 124 p.
128. **Ivar Kruusenberg.** Electroreduction of oxygen on carbon nanomaterial-based catalysts. Tartu, 2013, 191 p.
129. **Sander Piiskop.** Kinetic effects of ultrasound in aqueous acetonitrile solutions. Tartu, 2013, 95 p.
130. **Ilona Faustova**. Regulatory role of L-type pyruvate kinase N-terminal domain. Tartu, 2013, 109 p.
131. **Kadi Tamm.** Synthesis and characterization of the micro-mesoporous anode materials and testing of the medium temperature solid oxide fuel cell single cells. Tartu, 2013, 138 p.
132. **Iva Bozhidarova Stoyanova-Slavova.** Validation of QSAR/QSPR for regulatory purposes. Tartu, 2013, 109 p.
133. **Vitali Grozovski**. Adsorption of organic molecules at single crystal electrodes studied by *in situ* STM method. Tartu, 2014, 146 p.
134. **Santa Veikšina**. Development of assay systems for characterisation of ligand binding properties to melanocortin 4 receptors. Tartu, 2014, 151 p.
135. **Jüri Liiv.** PVDF (polyvinylidene difluoride) as material for active element of twisting-ball displays. Tartu, 2014, 111 p.
136. **Kersti Vaarmets.** Electrochemical and physical characterization of pristine and activated molybdenum carbide-derived carbon electrodes for the oxygen electroreduction reaction. Tartu, 2014, 131 p.
137. **Lauri Tõntson**. Regulation of G-protein subtypes by receptors, guanine nucleotides and Mn^{2+}. Tartu, 2014, 105 p.
138. **Aiko Adamson.** Properties of amine-boranes and phosphorus analogues in the gas phase. Tartu, 2014, 78 p.
139. **Elo Kibena**. Electrochemical grafting of glassy carbon, gold, highly oriented pyrolytic graphite and chemical vapour deposition-grown graphene electrodes by diazonium reduction method. Tartu, 2014, 184 p.
140. **Teemu Näykki.** Novel Tools for Water Quality Monitoring – From Field to Laboratory. Tartu, 2014, 202 p.
141. **Karl Kaupmees.** Acidity and basicity in non-aqueous media: importance of solvent properties and purity. Tartu, 2014, 128 p.

142. **Oleg Lebedev**. Hydrazine polyanions: different strategies in the synthesis of heterocycles. Tartu, 2015, 118 p.
143. **Geven Piir.** Environmental risk assessment of chemicals using QSAR methods. Tartu, 2015, 123 p.
144. **Olga Mazina.** Development and application of the biosensor assay for measurements of cyclic adenosine monophosphate in studies of G protein-coupled receptor signalinga. Tartu, 2015, 116 p.
145. **Sandip Ashokrao Kadam.** Anion receptors: synthesis and accurate binding measurements. Tartu, 2015, 116 p.
146. **Indrek Tallo.** Synthesis and characterization of new micro-mesoporous carbide derived carbon materials for high energy and power density electrical double layer capacitors. Tartu, 2015, 148 p.
147. **Heiki Erikson.** Electrochemical reduction of oxygen on nanostructured palladium and gold catalysts. Tartu, 2015, 204 p.
148. **Erik Anderson.** *In situ* Scanning Tunnelling Microscopy studies of the interfacial structure between Bi(111) electrode and a room temperature ionic liquid. Tartu, 2015, 118 p.
149. **Girinath G. Pillai.** Computational Modelling of Diverse Chemical, Biochemical and Biomedical Properties. Tartu, 2015, 140 p.
150. **Piret Pikma.** Interfacial structure and adsorption of organic compounds at Cd(0001) and Sb(111) electrodes from ionic liquid and aqueous electrolytes: an *in situ* STM study. Tartu, 2015, 126 p.
151. **Ganesh babu Manoharan.** Combining chemical and genetic approaches for photoluminescence assays of protein kinases. Tartu, 2016, 126 p.
152. **Carolin Siimenson**. Electrochemical characterization of halide ion adsorption from liquid mixtures at Bi(111) and pyrolytic graphite electrode surface. Tartu, 2016, 110 p.
153. **Asko Laaniste.** Comparison and optimisation of novel mass spectrometry ionisation sources. Tartu, 2016, 156 p.
154. **Hanno Evard.** Estimating limit of detection for mass spectrometric analysis methods. Tartu, 2016, 224 p.
155. **Kadri Ligi.** Characterization and application of protein kinase-responsive organic probes with triplet-singlet energy transfer. Tartu, 2016, 122 p.
156. **Margarita Kagan.** Biosensing penicillins' residues in milk flows. Tartu, 2016, 130 p.
157. **Marie Kriisa.** Development of protein kinase-responsive photoluminescent probes and cellular regulators of protein phosphorylation. Tartu, 2016, 106 p.
158. **Mihkel Vestli.** Ultrasonic spray pyrolysis deposited electrolyte layers for intermediate temperature solid oxide fuel cells. Tartu, 2016, 156 p.
159. **Silver Sepp**. Influence of porosity of the carbide-derived carbon on the properties of the composite electrocatalysts and characteristics of polymer electrolyte fuel cells. Tartu, 2016, 137 p.
160. **Kristjan Haav**. Quantitative relative equilibrium constant measurements in supramolecular chemistry. Tartu, 2017, 158 p.

161. **Anu Teearu**. Development of MALDI-FT-ICR-MS methodology for the analysis of resinous materials. Tartu, 2017, 205 p.
162. **Taavi Ivan**. Bifunctional inhibitors and photoluminescent probes for studies on protein complexes. Tartu, 2017, 140 p.
163. **Maarja-Liisa Oldekop**. Characterization of amino acid derivatization reagents for LC-MS analysis. Tartu, 2017, 147 p.
164. **Kristel Jukk**. Electrochemical reduction of oxygen on platinum- and palladium-based nanocatalysts. Tartu, 2017, 250 p.
165. **Siim Kukk**. Kinetic aspects of interaction between dopamine transporter and *N*-substituted nortropane derivatives. Tartu, 2017, 107 p.
166. **Birgit Viira**. Design and modelling in early drug development in targeting HIV-1 reverse transcriptase and Malaria. Tartu, 2017, 172 p.
167. **Rait Kivi**. Allostery in cAMP dependent protein kinase catalytic subunit. Tartu, 2017, 115 p.
168. **Agnes Heering**. Experimental realization and applications of the unified acidity scale. Tartu, 2017, 123 p.
169. **Delia Juronen**. Biosensing system for the rapid multiplex detection of mastitis-causing pathogens in milk. Tartu, 2018, 85 p.
170. **Hedi Rahnel.** ARC-inhibitors: from reliable biochemical assays to regulators of physiology of cells. Tartu, 2018, 176 p.
171. **Anton Ruzanov.** Computational investigation of the electrical double layer at metal–aqueous solution and metal–ionic liquid interfaces. Tartu, 2018, 129 p.
172. **Katrin Kestav.** Crystal Structure-Guided Development of Bisubstrate-Analogue Inhibitors of Mitotic Protein Kinase Haspin. Tartu, 2018, 166 p.
173. **Mihkel Ilisson.** Synthesis of novel heterocyclic hydrazine derivatives and their conjugates. Tartu, 2018, 101 p.
174. **Anni Allikalt.** Development of assay systems for studying ligand binding to dopamine receptors. Tartu, 2018, 160 p.
175. **Ove Oll.** Electrical double layer structure and energy storage characteristics of ionic liquid based capacitors. Tartu, 2018, 187 p.
176. **Rasmus Palm.** Carbon materials for energy storage applications. Tartu, 2018, 114 p.
177. **Jörgen Metsik.** Preparation and stability of poly(3,4-ethylenedioxythiophene) thin films for transparent electrode applications. Tartu, 2018, 111 p.
178. **Sofja Tšepelevitš.** Experimental studies and modeling of solute-solvent interactions. Tartu, 2018, 109 p.
179. **Märt Lõkov.** Basicity of some nitrogen, phosphorus and carbon bases in acetonitrile. Tartu, 2018, 104 p.
180. **Anton Mastitski**. Preparation of α-aza-amino acid precursors and related compounds by novel methods of reductive one-pot alkylation and direct alkylation. Tartu, 2018, 155 p.
181. **Jürgen Vahter**. Development of bisubstrate inhibitors for protein kinase CK2. Tartu, 2019, 186 p.

182. **Piia Liigand.** Expanding and improving methodology and applications of ionization efficiency measurements. Tartu, 2019, 189 p.
183. **Sigrid Selberg.** Synthesis and properties of lipophilic phosphazene-based indicator molecules. Tartu, 2019, 74 p.
184. **Jaanus Liigand.** Standard substance free quantification for LC/ESI/MS analysis based on the predicted ionization efficiencies. Tartu, 2019, 254 p.
185. **Marek Mooste.** Surface and electrochemical characterisation of aryl film and nanocomposite material modified carbon and metal-based electrodes. Tartu, 2019, 304 p.
186. **Mare Oja.** Experimental investigation and modelling of pH profiles for effective membrane permeability of drug substances. Tartu, 2019, 306 p.
187. **Sajid Hussain.** Electrochemical reduction of oxygen on supported Pt catalysts. Tartu, 2019, 220 p.
188. **Ronald Väli.** Glucose-derived hard carbon electrode materials for sodium-ion batteries. Tartu, 2019, 180 p.
189. **Ester Tee.** Analysis and development of selective synthesis methods of hierarchical micro- and mesoporous carbons. Tartu, 2019, 210 p.